Dopamine Activates Astrocytes in Prefrontal Cortex via α1-Adrenergic Receptors

Silvia Pittolo[1,2], Sae Yokoyama[1,3], Drew D. Willoughby[1,4], Charlotte R. Taylor[1,4], Michael E. Reitman[1,4], Vincent Tse[1], Zhaofa Wu[5], Roberto Etchenique[6], Yulong Li[5], Kira E. Poskanzer[1,4,7,8*]

[1] Department of Biochemistry & Biophysics, University of California, San Francisco, San Francisco, CA, USA

[2] Current address: Max Delbrück Center for Molecular Medicine in the Helmholtz Association, Robert-Rössle-Str. 10, 13125 Berlin, Germany

[3] Current address: Neuroscience Graduate Program, Princeton University, Princeton, NJ, USA

[4] Neuroscience Graduate Program, University of California, San Francisco, San Francisco, CA, USA

[5] State Key Laboratory of Membrane Biology, Peking University School of Life Sciences, Beijing 100871, China; Peking-Tsinghua Center for Life Sciences, Peking University, Beijing 100871, China

[6] Departamento de Química Inorgánica, Analítica y Química Física, INQUIMAE, Facultad de Ciencias Exactas y Naturales, Universidad de Buenos Aires, CONICET, Intendente Güiraldes 2160, Ciudad Universitaria, Pabellón 2, Buenos Aires (C1428EGA), Argentina

[7] Kavli Institute for Fundamental Neuroscience, San Francisco, CA, USA

[8] Lead contact

***Corresponding author:** Kira Poskanzer (kira.poskanzer@ucsf.edu)

Summary

The prefrontal cortex (PFC) is a hub for cognitive control, and dopamine profoundly influences its functions. In other brain regions, astrocytes sense diverse neurotransmitters and neuromodulators and, in turn, orchestrate regulation of neuroactive substances. However, basic physiology of PFC astrocytes, including which neuromodulatory signals they respond to and how they contribute to PFC function, is unclear. Here, we characterize divergent signaling signatures in mouse astrocytes of PFC and primary sensory cortex, which show differential responsiveness to locomotion. We find that PFC astrocytes express receptors for dopamine, but are unresponsive through the G_s/G_i-cAMP pathway. Instead, fast calcium signals in PFC astrocytes are time-locked to dopamine release, and are mediated by α1-adrenergic receptors both *ex vivo* and *in vivo*. Further, we describe dopamine-triggered regulation of extracellular ATP at PFC astrocyte territories. Thus, we identify astrocytes as active players in dopaminergic signaling in PFC, contributing to PFC function though neuromodulator receptor crosstalk.

Introduction

The prefrontal cortex (PFC) is a higher order association cortex that integrates sensory and cognitive information from other brain areas to execute behavior (Fuster et al., 2000). The PFC is involved in fundamental and diverse processes, including working memory and attention (Funahashi et al., 1989; Fuster and Alexander, 1971; Kesner et al., 1996), behavioral flexibility and planning (Dias et al., 1996; Ragozzino et al., 1999), and processing of stress, fear and emotions (George et al., 1995; Hariri et al., 2003; Kim et al., 2003; Milad and Quirk, 2002). Despite its importance, many aspects of PFC function remain poorly understood. For instance, whether persistent activity of individual PFC neurons or rather network dynamics underlie the ability of the PFC to hold information over multi-second delays during working memory tasks is subject of current debate (Barbosa et al., 2020; Cavanagh et al., 2018; Constantinidis et al., 2018; Inagaki et al., 2019; Park et al., 2019; Spaak et al., 2017).

While prefrontal circuits are fundamental for the top-down control of behavior, ascending arousal systems—including the mesocortical dopamine (DA) pathway—are so essential to PFC executive functions that their disruption recapitulates PFC lesions (Brozoski et al., 1979). Dopaminergic projections to PFC are particularly sensitive to stressful and aversive stimuli (Abercrombie et al., 1989; Lammel et al., 2012; Thierry et al., 1976; Vander Weele et al., 2018). However, how both phasic and tonic temporal patterns of DA play specific roles in PFC computations is unclear (Lohani et al., 2019), with evidence for bidirectional or opposing effects on the excitability of prefrontal neuron subtypes (Anastasiades et al., 2019; Chen et al., 2007; Gao and Goldman-Rakic, 2003; Gao et al., 2003; Huang et al., 2004; Kröner et al., 2007; Matsuda et al., 2006; Seamans et al., 2001; Vijayraghavan et al., 2007) which ultimately contribute to complex patterns of circuit activity underlying PFC functions.

Astrocytes—the most abundant non-neuronal brain cells—are well positioned to process neuronal signals, as they express receptors for neurotransmitters and neuromodulators (Porter and McCarthy, 1997) and have wide territories, each encompassing thousands of synapses (Bushong et al., 2002). Astrocytes are in a bidirectional dialogue with neurons, sensing neuronal activity through G protein-coupled receptors (GPCRs) (Kofuji and Araque, 2021), internally computing through Ca^{2+} and cAMP (Oe et al., 2020; Srinivasan et al., 2016), and regulating neuroactive substances such as glutamate (Bezzi et al., 2004; Yang et al., 2019) and ATP (Cao et al., 2013; Pascual et al., 2005; Zhang et al., 2003) that influence synaptic plasticity and network connectivity (Panatier et al., 2011; Perea and Araque, 2007; Poskanzer and Yuste, 2016). Impaired function of PFC astrocytes can cause depressive (Banasr and Duman, 2008; Cao et al., 2013; John et al., 2012; Lee et al., 2013) or autism-like behaviors (Wang et al., 2021), and interfere with working memory (Lima et al., 2014; Mederos et al., 2021; Petrelli et al., 2020; Sardinha et al., 2017). However, the mechanisms underlying astrocytic contributions to PFC are still largely unexplored.

Here, we use *in vivo* two-photon (2P) imaging, fiber photometry (FP), and *ex vivo* imaging of calcium (Ca^{2+}), cAMP, neuromodulators, and ATP to explore astrocyte signals in PFC. We first characterize Ca^{2+} dynamics of PFC astrocytes *in vivo*, and compare them to primary visual cortex (V1) astrocytes. We find that PFC astrocytes display unique spatiotemporal signals, and lack responsiveness to locomotion as opposed to sensory cortex (Paukert et al., 2014; Wang et al., 2019). We demonstrate that PFC astrocytes express dopamine receptors (DRs), but signal through fast, sustained Ca^{2+} mobilizations rather than canonical DR G_s/G_i-cAMP pathways. Unexpectedly, we find that DA in PFC elicits astrocyte activation through the G_q-coupled α1-AR both in acute slices and *in vivo*. Finally, we show that PFC astrocytes can regulate extracellular ATP (ATP_E) in response to DA. Together, our data demonstrate that PFC astrocytes sense neuromodulators and behavioral stimuli differently than sensory cortical astrocytes. By exploring the physiology of PFC astrocytes, we uncover functional crosstalk between DA and receptors for norepinephrine (NE).

Results

PFC astrocytes exhibit single-cell restricted Ca^{2+} activity

Since PFC is an associative cortical area (Fuster et al., 2000), we hypothesized that astrocyte Ca^{2+} in PFC may have unique properties compared to primary sensory cortex, where population-level bursts of activity are well documented (Bekar et al., 2008; Ding et al., 2013; Slezak et al., 2019; Srinivasan et al., 2016; Wang et al., 2019). To test this, we compared spontaneous astrocyte Ca^{2+} activity in PFC and V1 using 2P microscopy in head-fixed mice. We implanted either a GRIN lens (Levene et al., 2004) over PFC or a cranial window over V1 in mice expressing Lck-GCaMP6f (Fig 1A) (Shigetomi et al., 2010;

Srinivasan et al., 2016) under the astrocyte-specific promoter *GfaABC$_1$D*. GRIN lens positioning was confirmed post-mortem and GFAP staining confirmed low astrocyte reactivity around the implant (Fig S1).

Using event-based image analyses (Wang et al., 2019), the largest astrocyte Ca^{2+} signals in PFC often appeared the size of a single astrocyte (~50×50μm; Fig 1B–C top), whereas the population-level, burst-like events in V1 span the entire imaging field (300×300μm; Fig 1B–C bottom, Slezak et al., 2019; Srinivasan et al., 2016; Wang et al., 2019). We focused on these larger events (>1000 μm^2) for comparison (Fig 1D–H), and found that while astrocyte Ca^{2+} events occur at the same rate in PFC and V1 (Fig 1D), they are smaller (Fig 1E) and last longer (Fig 1F) in PFC. We found that Ca^{2+} events in PFC are less synchronous with other PFC events (Fig 1G), but repeat more at the same locations in the imaging field compared to those in V1 (Fig 1H). Although less obvious, smaller Ca^{2+} events (<1000μm^2) also differ between PFC and VI (Fig S1C–G). These data indicate that Ca^{2+} dynamics may be driven by different mechanisms depending on brain region, and suggest that PFC astrocytes may play different functional roles than in primary sensory cortex.

Population-level astrocyte Ca^{2+} activity in PFC is not tightly linked to locomotion

Since burst-like astrocyte Ca^{2+} in V1 is locomotion-driven (Paukert et al., 2014; Slezak et al., 2019; Wang et al., 2019), we next wondered whether differences in Ca^{2+} in PFC and V1 were due to differences in responses to locomotion (Video 1). To examine this, we aligned population-level astrocyte Ca^{2+} traces to locomotion onsets (Fig 1J–K and Fig S1H–I). Average astrocyte Ca^{2+} in V1 significantly increases soon after locomotion onset (Fig 1K left, green, Paukert et al., 2014; Slezak et al., 2019). By plotting the distribution of time of maximum change in Ca^{2+} (Fig 1K, right), we observe a peak 6–9s after locomotion onset. In contrast, PFC astrocytes did not exhibit significant and sustained Ca^{2+} increases at locomotion onset, and no clear peak for maximum change across trials is evident (Fig 1K, red). These results indicate that PFC astrocytes are not activated by locomotion on average, although we do not exclude the possibility that a few astrocytes or domains are locomotion-linked. To explore whether Ca^{2+} in PFC astrocytes is instead involved in locomotion generation, we aligned locomotion traces to Ca^{2+} event onset (Fig 1L–M, Fig S1J–K), and found no times when speed significantly deviated from average (Fig 1M left, red). When mice moved, the maximum speed was equally distributed over the time window around Ca^{2+} event onsets (Fig 1M, right), suggesting that PFC Ca^{2+} activity is unlinked from locomotion. In contrast, Ca^{2+}-aligned locomotion analysis in V1 shows that speed increases starting at -5.1s before Ca^{2+} event onset and until 2.2s after, and peaks -1.1s before Ca^{2+} onset (Fig 1M left, green), in accordance with previous observations (Fig 1J–K). These results indicate that astrocyte activity in PFC differs significantly from that in V1, both in Ca^{2+} event dynamics and their relationship with locomotion.

PFC astrocytes express DRs

Because burst-like astrocyte population dynamics are mediated by NE (Bekar et al., 2008; Ding et al., 2013; Paukert et al., 2014) and PFC astrocytes do not display bursting (Fig 1B–C), we wondered whether DA—a neuromodulatory input for PFC neurons (Brozoski et al., 1979; Thierry et al., 1976)—is involved in PFC astrocyte Ca^{2+} activity *in vivo*. To explore this, we examined DR expression in PFC astrocytes by crossing transgenic reporter lines *Drd1a*-tdTomato (Shuen et al., 2008) or *Drd2*-EGFP (Gong et al., 2003) to the astrocyte-specific reporter lines *Aldh1l1*-EGFP (Tsai et al., 2012) or *Aldh1l1*-tdTomato (Gong et al., 2003) (Fig 2A). We immunostained for the fluorophores and determined colocalization in cell somata across PFC layers (Fig 2C–D and Fig S2A), finding that 13±1% of all Aldh1l1$^+$ cells colocalize with D_1 and 14±1% colocalize with D_2 (Fig 2C). Conversely, 18±2% of all D_1^+ cells and 41±3% of all D_2^+ cells are Aldh1l1$^+$ (Fig 2D). For both receptors, colocalization with Aldh1l1 was maximal in layer 1, consistent with mostly neuronal projections rather than somata in the most superficial layer. These results demonstrate expression of D_1 and D_2 in PFC astrocytes, suggesting that PFC astrocytes may respond specifically to DA, as in other brain regions (Chai et al., 2017; Corkrum et al., 2020; Cui et al., 2016; Fischer et al., 2020; Jennings et al., 2017; Xin et al., 2019).

Direct DR stimulation does not recruit cAMP intracellular signaling

D1-like ($D_{1/5}$) and D2-like ($D_{2/3/4}$) receptors (hereafter D1R and D2R) are canonically coupled to G_s- and G_i-GPCR proteins, respectively. To test whether these receptors in PFC astrocytes lead to changes in cAMP, we expressed the fluorescent cAMP reporter Pink Flamindo (Harada et al., 2017) in PFC astrocytes and performed acute slice experiments (Fig 2E) while pharmacologically targeting DRs (Fig 2F–G). We blocked possible contributions from neighboring D1R- and D2R-expressing neurons by inhibiting action potentials (TTX) and preventing neuron-to-astrocyte signaling (multi-drug cocktail, Methods). We bath-applied 10μM DA to reflect physiological levels (Fig 2F left, top), and did not observe changes in average Pink Flamindo fluorescence (Fig 2G). However, because D1R and D2R have opposing effects on adenylate cyclase (AC), DA could in principle both stimulate and inhibit cAMP. We searched at the single-cell level for increases or decreases in cAMP, and still did not observe changes with DA (Fig S2B).

To distinguish between contributions of G_s and G_i signaling, we next directly activated either D1R or D2R with subtype-specific agonists (D1R: SKF81297, 10μM; D2R: Quinpirole, 10μM) and imaged cAMP (Fig 2F left, middle–bottom). Again, we found no change in average cAMP with either drug (Fig 2G). To confirm that Pink Flamindo detects cAMP changes, we followed each experiment with bath-application of the AC agonist Forskolin (10μM, Fig 2F right). Forskolin led to consistent increases in

Pink Flamindo fluorescence relative to both baseline and drug treatment (Fig 2G, Fig S2B), which was comparable to Forskolin stimulation in naïve slices (-TTX and drug cocktail; Fig S2C). We confirmed that these results were not due to slice-to-slice variability (Fig 2G) or cell-to-cell differences in Pink Flamindo expression (Fig S2D), indicating that neither DA nor DR subtype-specific agonists induce detectable changes downstream of G_s or G_i effector proteins in PFC astrocytes.

DA activates PFC astrocyte Ca^{2+} signals via cell-surface ARs

To test whether DA mobilizes intracellular Ca^{2+} rather than cAMP in PFC astrocytes—and may be mediating *in vivo* Ca^{2+} activity (Fig 1)—we expressed GCaMP6f in PFC astrocytes using viruses (Fig 3A–B) and carried out bath-application experiments in acute slices, blocking neuronal activity as above. DA bath-application caused an increase in Ca^{2+} event frequency compared to baseline (Video 2; Fig 3C–D, and Fig 3E pink). In contrast, application of D1R and D2R agonists (SKF38393 and Quinpirole, 10μM) had no discernible effect on Ca^{2+} (Fig 3E, yellow; Fig S3A top left). To test whether DRs are engaged in DA-dependent increases in Ca^{2+}, we next bath-applied DA in the presence of DR antagonists SCH23390 and Sulpiride, and observed partial inhibition of Ca^{2+} dynamics (Fig S3A, top right), although no significant decrease in event rate compared to DA alone (Fig 3D, blue).

Since the effect of DA on Ca^{2+} is minimally inhibited by DR antagonists, we next tested whether the robust response to DA is mediated by GPCRs by adding DA to slices from mice genetically lacking IP_3R2 (Li et al., 2005), the main intracellular receptor downstream of GPCRs in astrocytes mediating intracellular Ca^{2+} release (Petravicz et al., 2008; Zhang et al., 2014). In these slices, we observed significant inhibition of Ca^{2+} mobilization by DA (Fig 3D, gray and Fig S3A, bottom left), suggesting that PFC astrocytes indeed rely on GPCRs to mediate the Ca^{2+} response. Because DA can act on ARs in neurons (Alachkar et al., 2010; Cilz et al., 2014; Cornil et al., 2002; Guiard et al., 2008; Marek and Aghajanian, 1999; Özkan et al., 2017), we next carried out DA-application in the presence of broad-spectrum AR antagonists (α1/α2: Phentolamine; β: Propranolol; 10μM). In contrast to DR antagonists, blocking ARs completely abolished DA-mediated increase in Ca^{2+} activity (Fig 3C, green and Fig S3A, bottom right).

Because Ca^{2+} activity by bathed DA had a slow onset and was sensitive to AR inhibitors, we thought that DA may be transformed to NE, a one-step enzymatic product of DA (Kirshner, 1957). To confirm that PFC astrocytes were indeed responding to DA and not NE, we imaged acute PFC slices in which the fluorescent sensor $GRAB_{NE}$ was expressed throughout the tissue (Fig 3F), and bath-applied either DA or NE. DA did not induce a significant change in $GRAB_{NE}$, in contrast to a large response to NE (Fig 3G), suggesting that the response to DA mediated by ARs (Fig 3C) is not linked to conversion of DA to NE. Lastly, we tested whether DA induced Ca^{2+} via GPCR signaling from the plasma membrane, or via

intracellular compartments, since GPCR signaling can occur via internal organelles (Calebiro et al., 2009; Irannejad et al., 2013; Kotowski et al., 2011) and DR antagonists display low membrane-permeability (Dos Santos Pereira et al., 2014). To do this, we imaged PFC astrocyte Ca^{2+} (using Fluo-4) in organic cation transporter 3 knockout mice ($OCT3^{-/-}$, Fig 3H), in which intracellular transport of monoamines is blocked (Amphoux et al., 2006; Cui et al., 2009; Duan and Wang, 2010; Zwart et al., 2001). DA bath-application in these slices (Fig 3I, left) led to a robust increase in Fluo-4 fluorescence (Fig 3I right), suggesting that DA acts on cell-surface GPCRs in PFC astrocytes.

Physiological concentrations of DA evoke fast Ca^{2+} transients in PFC astrocytes

The previous experiments demonstrated that PFC astrocytes respond to continuous DA application with slow-onset Ca^{2+} transients. We next explored whether astrocytes can be engaged by acute stimuli better reflecting physiological DA dynamics. To do so, we used one-photon (1P) activation of a caged DA (RuBi-DA, Fig 4A–B) (Araya et al., 2013) to achieve fast release and mimic volume transmission (Agnati et al., 1995; Banerjee et al., 2020), the main modality of PFC DA release. We validated our light-stimulation protocol with the fluorescent DA sensor dLight (Patriarchi et al., 2018) by comparing a DA dose-response curve (Fig 4C and Fig S4A) to photoactivation of RuBi-DA (Fig 4D and Fig S4B left). We estimate that uncaging released ~2µM DA (Fig 4E), matching DA levels detected by voltammetry in PFC *in vivo* (Garris and Wightman, 1994) and DA concentration estimates near release sites in other areas (Courtney and Ford, 2014; Patriarchi et al., 2018).

To understand how single PFC astrocytes respond to temporally controlled DA release, we uncaged RuBi-DA in slices with GCaMP-expressing astrocytes (Fig 4F top, Video 3) while blocking neurons as above. We drew borders around each cell (Fig 4F, bottom) and detected Ca^{2+} events (Fig 4G–I) to monitor the area within cells recruited over time (Fig 4J–L). In control conditions (no RuBi-DA; Fig 4G–H, left), most cells (91%) were inactive throughout the trial and similar numbers increased or decreased Ca^{2+} activity around the light pulse (4%). In RuBi-DA (Fig 4G–H, right), most cells across cortical layers responded to uncaging with increased (62%) rather than decreased (4%) activity. In individual cells, events were more abundant, larger, and lasted longer following light stimulation in RuBi-DA, but not in controls (Fig 4I). These results were not affected by the pharmacological cocktail used since all features of Ca^{2+} events were unchanged compared to naïve slices (Fig S4C–D).

Overall, Ca^{2+} mobilization in individual astrocytes (Fig 4K) was induced with a short onset time (8.6s, Fig 4K, L, left) and short duration (9.9s, Fig 4K, middle), whereas the area of the cell recruited varied considerably among cells (49%, Fig 4K, right). These results were not affected by our single-cell delineation method, as no correlation between cell size and area of cell recruited by DA was seen (Fig

S4E). These data demonstrate that astrocytes respond acutely to physiological DA levels with fast, transient Ca^{2+} dynamics covering variable astrocyte territories.

PFC astrocytes require α1-AR signaling for DA response

We next photoreleased DA on PFC slices treated with subtype-specific inhibitors of DRs or ARs (Fig 5A, Video 4). As before (Fig 4), we observed an increase in Ca^{2+} following uncaging of RuBi-DA alone (Fig 5B–C, pink; control). Antagonizing D1R or D2R did not occlude the response to DA (Fig 5B–C), in accordance with bath-application data (Fig 3E) and further supporting the idea that DRs are not involved in the recruitment of PFC astrocytes by DA. Next, we tested the contribution of all AR subtypes (α1, α2 and β) to DA-mediated Ca^{2+} activity, and found that only inhibition of α1-AR prevented Ca^{2+} mobilization after DA photorelease (Fig 5B–C). We also measured astrocyte activity using different metrics (Fig S5A–B) and found no change from the above results. Overall, these data suggest that fast, volume transmission-like release of DA at physiological concentrations recruits PFC astrocytes via α1-ARs.

DA evokes Ca^{2+} signals in PFC astrocytes via α1-ARs in vivo

To test whether DA input to PFC induces astrocyte activity *in vivo*, we carried out dual-color FP recordings using viral expression of the red-shifted Ca^{2+} sensor jR-GECO1b and the DA sensor dLight (Fig 6A and Fig S6E). Because aversive stimuli such as foot shock (Thierry et al., 1976), tail shock (Abercrombie et al., 1989), and tail pinch (Vander Weele et al., 2018) activate the mesocortical DA system, we used an aversive tail-lift stimulus (Hurst and West, 2010) to increase DA levels in PFC. Using this experimental paradigm and monitoring extracellular DA, we found that this was indeed the case (Fig 6A, green). jR-GECO1b signals also showed large astrocyte Ca^{2+} transients during the tail-lift (Fig 6A, pink). Aligning transients from these channels showed that jR-GECO closely followed dLight (Fig 6B–C and Fig S6A). Cross-correlation indicated that dLight precedes the jR-GECO signal by 1.4s (Fig 6D), suggesting that extracellular DA contributes to the PFC astrocyte Ca^{2+} that follows aversive stimuli.

Because aversion also releases NE in PFC (Gresch et al., 1994), we next sought to describe any contribution of NE to this close relationship between DA and astrocyte Ca^{2+} *in vivo*. To do this, we carried out dual-color FP experiments after injection of DSP4 (Fig 6E), a toxin that specifically ablates locus coeruleus (LC) projection fibers (Bekar et al., 2008; Ding et al., 2013; Fritschy and Grzanna, 1989), the main source of PFC NE. We confirmed that DSP4 reduced LC fibers in PFC by NE transporter (NET) immunostaining after treatment (Fig 6F), and again compared dLight and jR-GECO. DA signal amplitude in response to the aversion paradigm was unchanged in astrocytes of NE-depleted mice compared to controls (Fig S6B, left), supporting the selectivity of the toxin in targeting LC fibers. In addition, while

we observed a decrease in astrocyte Ca^{2+} amplitude (Fig S6B, right)—consistent with NE effects elsewhere (Bekar et al., 2008; Ding et al., 2013; Gordon et al., 2005; Paukert et al., 2014)—Ca^{2+} transients co-occurring with dLight transients remained evident after NE depletion (Fig S6A, middle row). These Ca^{2+} signals were longer (18s, Fig S6C), and occurred with longer lag after dLight (2.6s, Fig S6D) compared to untreated animals (duration 7s, lag 1.4s), which may be explained by slower DA uptake in the absence of NET (Morón et al., 2002; Sesack et al., 1998). These results indicate that mesocortical DA can recruit PFC astrocytes during an aversive stimulation, independent of LC input.

To test the possible crosstalk of DA and α1-ARs *in vivo*, we next compared responses to aversive stimulation in mice treated with DSP4 before and after injection of the bioavailable α1-AR antagonist Prazosin (Fig 6G–H). While dLight signals in response to aversion were maintained after Prazosin (Fig 6G, left), Ca^{2+} dynamics were significantly reduced (Fig 6G, right) and did not follow DA dynamics (Fig 6H). Together, these data suggest that α1-AR signaling accounts for the bulk of the astrocyte Ca^{2+} response to DA in PFC *in vivo*.

DA increases ATP_E at PFC astrocytes

DA stimulates ATP release from *nucleus accumbens* astrocytes (Corkrum et al., 2020). To test whether α1-AR-mediated activation of PFC astrocytes by DA leads to ATP_E mobilization, we performed acute slice experiments on astrocytes expressing a fluorescent ATP sensor ($GRAB_{ATP}$, Fig 7A–C; Wu et al., 2021). We determined the response dynamics of the sensor by bathing on exogenous ATP (50μM, Fig 7B–C). Continuous ATP stimulation led to an increased event rate (Fig 7D), with events whose size matched the territory of individual astrocytes and could be detected during the entire course of the ATP application (Fig 7E), showing that $GRAB_{ATP}$ reliably detects ATP_E over the entire astrocyte surface for prolonged periods.

We next repeated $GRAB_{ATP}$ experiments while bath-applying DA (10μM, Fig 7F–H) and blocking neuronal contributions as above (without PPADS and CGS 15943 to avoid occluding $GRAB_{ATP}$ fluorescence changes, Methods). DA induced mobilization of ATP_E (Fig 7H) and increased ATP event frequency (Fig 7I). These sparse, DA-induced events lasted ~30s and did not encompass the entire astrocyte territory (Fig 7J), indicating that ATP is increased at specific cellular locations at PFC astrocytes in response to DA. When adding Doxazosin before each recording to inhibit α1-ARs (Fig 7K), the frequency of ATP_E events after addition of DA no longer increased (Fig 7M–N), but the area and duration of the spontaneous events were similar to those observed with DA alone (Fig 7L, O), supporting the concept that α1-ARs are important for DA signaling that leads to ATP increases. Although we do not rule

out the contribution of other cell types to this phenomenon, this relationship between DA signaling and ATP may contribute to regulation of synaptic transmission in PFC.

Discussion

PFC astrocyte function in vivo

Astrocytes play active roles in computation and behavior, including in PFC (Mederos et al., 2021). We find that PFC astrocytes differ in neurophysiology from those in sensory cortex (Fig 1). They are activated with different spatiotemporal patterns of intracellular Ca^{2+} (Fig 1), and when animals are exposed to aversive stimuli (Fig 6), but not in response to locomotion (Fig 1). These results are consistent with PFC neuronal network involvement in stress processing (Abercrombie et al., 1989; Lammel et al., 2012; Rosenkranz and Grace, 2001; Thierry et al., 1976; Vander Weele et al., 2018), with changes in astrocytes following stress (Abbink et al., 2019; Bender et al., 2020; Murphy-Royal et al., 2020; Simard et al., 2018), and with divergent transcriptomic, morphological, and cellular signaling landscapes in astrocytes of different brain areas (Batiuk et al., 2020; Chai et al., 2017; Khakh and Sofroniew, 2015; Xin et al., 2019), to support the hypothesis that astrocytes serve specific functions in PFC.

DA actions on PFC astrocytes: sustained and heterogeneous responses

Compared to subcortical areas (Abercrombie et al., 1989; Garris and Wightman, 1994), spatial diffusion and temporal availability of DA in PFC are extended due to faster firing (Lammel et al., 2008) and lower reuptake rates (Sesack et al., 1998), resulting in complex effects on PFC circuits (Lohani et al., 2019). Astrocytes respond with Ca^{2+} to DA in non-cortical brain areas (Chai et al., 2017; Corkrum et al., 2020; Cui et al., 2016; Fischer et al., 2020; Jennings et al., 2017; Xin et al., 2019), and our study expands this knowledge to PFC, demonstrating further that astrocytes can respond to both continuous (Fig 3) and phasic release (Fig 4) of DA. The different dynamics of PFC astrocyte Ca^{2+} observed in response to these two modes of DA delivery suggest a possible mechanism by which astrocytes discern between tonic and phasic DA signals, which are integral to PFC function. Since in *ex vivo* experiments, we blocked action potentials and neuronally released molecules known to bind astrocytic GPCRs, our data demonstrate that PFC astrocytes respond to DA directly, i.e. independently of neuronal activation. This indicates that astrocytes actively contribute to the dopaminergic control of PFC.

Our uncaging data (Fig 4) show that, even in the absence of neuronal DA responses, rapid release of physiological levels of DA recruits astrocyte responses in seconds, which are sustained for tens of seconds in most cells. Individual astrocyte responses, rather than population-wide activity, demonstrate that the extent of subcellular locations engaged in Ca^{2+} signaling following DA release differs across PFC astrocytes. These observations suggest that astrocytes may be involved in regulation of sustained activity, and contribute to local PFC computations in a cell-specific manner.

DA actions on PFC astrocytes: receptors and signaling pathways

Our results demonstrating that DA acting on PFC astrocytes recruits Ca^{2+} (Fig 3–4) rather than cAMP (Fig 2) are in contrast with neuronal research showing that DA activates G_s/G_i-cAMP pathways canonically ascribed to D1R and D2R (Lee et al., 2021; Muntean et al., 2018; Nomura et al., 2014; Yapo et al., 2017), but in agreement with evidence that DA activates astrocytic G_q-IP_3- Ca^{2+} pathway elsewhere (Chai et al., 2017; Corkrum et al., 2020; Cui et al., 2016; Fischer et al., 2020; Jennings et al., 2017; Xin et al., 2019). These results suggest differential expression of signaling machinery components across cell types. However, pharmacology data (Fig 3, 5–6) support the idea that lack of cAMP mobilization is due to DA acting on PFC astrocytes exclusively through α1-AR, even though PFC astrocytes express D_1 and D_2 (Fig 2). Indeed, our data that PFC astrocytes respond to DA by α1-ARs differs from previous astrocytic research in other brain regions, in which DA changes Ca^{2+} via DRs (Corkrum et al., 2020; Fischer et al., 2020; Jennings et al., 2017). However, it is consistent with studies of neuronal activation by DA showing that DR agonists or antagonists are unable to reproduce or prevent effects of DA (Cilz et al., 2014; Cornil and Ball, 2008; Cornil et al., 2002; Guiard et al., 2008; Marek and Aghajanian, 1999; Nicola and Malenka, 1997; Özkan et al., 2017). Further, our data could help reconcile apparently contradictory findings whereby different modes of DA activation (i.e. DA versus synthetic agonists) lead to contrasting results in astrocytes even within brain regions (Corkrum et al., 2020; D'Ascenzo et al., 2007). For instance, dorso-ventral or layer-specific gradients of VTA/LC innervation or DR/AR expression in hippocampus (Edelmann and Lessmann, 2018) could have influenced responses observed by Jennings *et al*., whereby lower local expression of DRs in *stratum lacunosum-moleculare* could have allowed AR-mediated DA responses to take over, explaining a lack of sensitivity to DR antagonists. Similarly, because the transcriptomic, morphological, and signaling landscape of astrocytes can diverge across cortical layers or brain areas (Batiuk et al., 2020; Chai et al., 2017; Lanjakornsiripan et al., 2018; Xin et al., 2019), region- or subregion-specific patterns of innervation and receptor expression could favor different mechanisms of DA activation and explain lack of activation by D1/D2 agonists in some studies (Chai et al., 2017; D'Ascenzo et al., 2007), and lack of inhibition by DR antagonists in others (Jennings et al., 2017).

DA/α1-AR promiscuity

We show that astrocytic DA signaling is subject to receptor promiscuity, a finding supported by research reporting that neuronal effects of DA could not be reproduced with DA-selective agonists (Cilz et al., 2014; Nicola and Malenka, 1997; Özkan et al., 2017), or could be prevented by α-AR, but not DR, antagonists (Cilz et al., 2014; Cornil et al., 2002; Guiard et al., 2008; Marek and Aghajanian, 1999; Özkan et al., 2017). Further, many levels of interaction between dopaminergic and noradrenergic systems have been documented in PFC: DA and NE are co-released by LC fibers (Devoto et al., 2005), DA uptake

occurs mainly by NET (Morón et al., 2002), and sub- or supra-threshold stimulation of both systems leads to detrimental outcomes on PFC performance (Arnsten et al., 2012). Together, this indicates that DA may interact with the noradrenergic system at receptor- and signal transduction-levels on PFC astrocytes. However, despite likely acting through the same astrocytic receptors, DA and NE show markedly different Ca^{2+} mobilization signatures: DA evokes high-frequency events small in amplitude and duration (Fig 3), while NE causes big amplitude and short duration events (Pankratov and Lalo, 2015). Thus, DA-AR crosstalk does not implicate information loss, as astrocytes may implement different effects downstream of specific inputs, through combinations of receptors recruited, their stoichiometry, and positions relative to effectors.

How this promiscuity originates at the receptor level is an exciting follow-up area. For example, does DA bind directly to α1-ARs and stimulate Ca^{2+} independently from DRs, or does DA induce a physical interaction between the bound DR and α1-AR, which then drives downstream Ca^{2+}? While radioligand binding studies indicate that non-specific interaction of DA with α1-AR only occurs at sub-mM concentrations (Proudman and Baker, 2021; Steinberg and Bilezikian, 1982), D_1 and α1-AR colocalize on PFC dendrites and may undergo co-trafficking (Mitrano et al., 2014). Further, co-immunoprecipitation, BRET/FRET sensors and proximity-ligation assays support the idea that DRs can form functional heteromeric complexes with ARs (González et al., 2012; Rebois et al., 2012).

Many drugs for psychiatric disorders such as depression, anxiety, ADHD, and schizophrenia target multiple monoamine systems (Stanford and Heal, 2019). Astrocytes have been linked to ADHD (Nagai et al., 2019), and methylphenidate—a therapy for ADHD—increases both DA and NE concentration by blocking DAT and NET (Berridge et al., 2006). Our results highlight open questions about these treatments: are both neuromodulators needed for therapeutic outcomes, or both involved in adverse effects? Do DA and NE act differently on neurons or non-neuronal cells? Are both DRs and ARs required to transduce DA signals in astrocytes, and would drugs that specifically target this interaction achieve better outcomes and minimize side effects? Clarifying the interactions between DA and ARs will be key for understanding treatments involving both catecholamine systems.

PFC DA, astrocytes and ATP

ATP is released by astrocytes in other brain areas in response to DA (Corkrum et al., 2020) and other neurotransmitters (Gordon et al., 2005; Lalo et al., 2014; Pougnet et al., 2014), and can lead to synaptic depression (Corkrum et al., 2020; Martin-Fernandez et al., 2017; Pascual et al., 2005; Zhang et al., 2003). Because we observe regulation of ATP_E in response to DA during neuronal blockade (Fig 7), and PFC astrocytes can release ATP (Cao et al., 2013), DA may favor suppression of PFC activity over long timescales through astrocyte-derived ATP, such as during delay periods of working memory tasks. Here, DA induces spatially restricted patterns of ATP_E, suggesting that astrocytes could depress activity of

specific synapses located within their territories. Future work could explore whether PFC astrocytes regulate ATP_E at defined neuronal subtypes or synapses to coordinate specific microcircuits.

Limitations of the study

We show that PFC astrocytes differ from V1 astrocytes in relation to locomotion, as an example of a simple behavior. Further studies are needed to explore astrocytic function relative to complex behaviors and test whether our results are unique to PFC. While the present work shows that ARs are required as a functional link between DA and PFC astrocytes, DA could also target non-astrocytic ARs, and further work could clarify whether this crosstalk occurs in other cell types or brain regions.

Acknowledgements

The authors are grateful to the Poskanzer lab for helpful discussions, especially Michelle Cahill for *ex vivo* analysis. We thank the Bender lab (UCSF) and Yuste lab (Columbia University) for reagent assistance, Victoria Cheung in the Feinberg lab (UCSF) for FP set up, Hajime Hirase (University of Copenhagen) for Pink Flamindo, and Jennifer Thompson for administrative support. K.P. is supported by NIH R01NS099254, NIH R01MH121446, NIH R21DA048497, and NSF CAREER 1942360. S.P. is supported by the EU under the Horizon 2020 Marie Skłodowska Curie Actions project ASTRALIS, GA 839561. M.R. was supported by the UCSF Genentech Fellowship. R.E. is a member of CONICET.

Author Contributions

Conceptualization, S.P. and K.E.P.; Methodology, S.P., S.Y., and K.E.P.; Formal Analysis, S.P.; Investigation, S.P., S.Y., D.D.W., C.R.T., M.E.R., V.T.; Resources, Z.W., R.E., Y.L.; Writing – Original Draft, S.P. and K.E.P.; Writing – Review & Editing, S.P. and K.E.P.; Supervision, S.P. and K.E.P.; Funding Acquisition, S.P. and K.E.P.

Declaration of Interests

The authors declare no competing interests.

Main figure titles and legends

Figure 1: PFC astrocytes exhibit region-specific Ca^{2+} activity. (A) Schematic for *in vivo* head-fixed 2P imaging of astrocyte Ca^{2+} in PFC (via GRIN lens) or V1 (cranial window). **(B)** Representative frames of astrocytic GCaMP6f in PFC (top) or V1 (bottom), relative to Ca^{2+} event onset. **(C)** Two examples of large AQuA-detected Ca^{2+}-events each in PFC (red, top) and V1 (green, bottom). Fields-of-view=300x300μm^2. To the right of each image is corresponding time-course of all detected events within 10s, with the onset time of the largest event at t=0 and solid line indicating frame displayed at left. Events <1000μm^2 in gray. **(D–H)** Large astrocyte Ca^{2+}-event features vary between brain regions. Events occur at similar rates in PFC and V1 (D), but in PFC are (E) smaller and (F) longer than in V1. PFC events (G) co-occur with other events less than in V1, but (H) tend to repeat more at the same location. All bins/events (colored dots), 5^{th}–95^{th} percentile distribution (violins), and mean±sem (black dots and error bars). Event rate (min^{-1}): 0.38±0.05 (PFC), 0.42±0.08 (V1); area (μm^2): 2422±190 (PFC), 6639±1346 (V1); duration (s): 12.6±1.1 (PFC), 9.4±0.5 (V1); temporal co-occurrence: 1.06±0.03 (PFC), 1.87±0.13 (V1); spatial co-occurrence: 4.7±0.5 (PFC), 2.9±0.3 (V1). Wilcoxon rank-sum test; *, $p<0.05$; $p=0.629$ (frequency), $p=0.012$ (area), $p=0.012$ (duration), $p<10^{-4}$ (co-occurring), $p=0.034$ (co-localized). PFC: n=180 60-s bins, 68 events, 4 mice; V1: n=130 60-s bins, 55 events, 3 mice. **(I–M)** Locomotion does not induce population-wide astrocyte Ca^{2+} in PFC. (I) Example time-course of normalized astrocyte Ca^{2+} (colored trace, top) and corresponding mouse speed (black, bottom). (J–K) Astrocyte Ca^{2+} traces aligned to locomotion onset (t=0), shown as heatmaps for all recordings (J), average traces±sem (K, left) and binned distribution of maximum Ca^{2+} change (K, right). In (K), line above traces indicates significant change from average Ca^{2+} at t<0. Shuffle test, 10000 pair-wise shuffles; $p<0.01$, Bonferroni correction for multiple comparisons. PFC: n=84 bouts, 4 mice; V1: n=77 bouts, 3 mice. (L–M) Animal speed aligned to onset of astrocyte Ca^{2+} events (t=0), shown as heatmap for all recordings (L), average traces±sem (M, left), and binned distribution of maximal speed (M, right). In (M), line above traces indicates significant increase above average speed for entire window. Shuffle test, 10000 pair-wise shuffles; $p<0.01$, Bonferroni correction for multiple comparisons. PFC: n=424 events, 4 mice; V1: n=1501 events, 3 mice.

Figure 2: D_1 and D_2 are expressed by PFC astrocytes but do not recruit G_s/G_i pathways. (A) Transgenic crosses to identify co-expression of D_1 (left column, top) or D_2 (right column, top) with astrocytic Aldh1l1 (middle row). Whole-brain coronal sections containing PFC. **(B)** Example of marker colocalization in PFC of *Drd1*-tdTomato x *Aldh1l1*-GFP mouse. Arrowheads indicate astrocytes co-expressing D_1 (magenta) and Aldh1l1 (green). Boundaries between cortical layers indicated by dashed lines. **(C–D)** Percentage of (C) Aldh1l1$^+$ astrocytes expressing D_1 (Drd1$^+$, magenta) and D_2 (Drd2$^+$, green), and of (D) Drd1$^+$ (magenta) and Drd2$^+$ (green) cells that co-express Aldh1l1 in PFC. Mean±sem; n=3 sections/mouse, 3 (D_1) and 2 (D_2) mice. **(E)** Schematic for 2P cAMP imaging in acute PFC slices. Micrographs show Pink Flamindo expression in entire field-of-view (top), and 3 cells with astrocyte morphology (bottom). **(F)** DR agonists (colors) do not mobilize whole-cell cAMP in PFC astrocytes. AC activator Forskolin (black) in the same slices confirms Pink Flamindo activity. Boxes on traces indicate 20-s windows used for quantification in (G). Traces shown as slice averages±sem of whole-cell changes in Pink Flamindo intensity (dF/F); n=110–180 cells, 7–8 slices, 7–8 mice. **(G)** Quantification of (F) at time-points indicated by small boxes, shown as box plots indicating mean and 10^{th}–90^{th} percentile, and error bars indicating minima and maxima. Slice mean±sem (Control, +Drug, +Forskolin): -0.003±0.004, 0.02±0.01, 0.24±0.03 (DA); 0.003±0.002, 0.006±0.007, 0.13±0.01 (D1); 0.003±0.002, 0.016±0.007, 0.18±0.03 (D2). Friedman test after Levene test; n.s., $p>0.05$, **, $p<0.01$; not shown on graph are comparison between Drug and Forskolin ($p<0.05$ for all agonists), and comparisons within conditions (controls, Drugs, or Forskolins; one-way Anova or Kruskal-Wallis after Levene test, all $p>0.05$); n=110–180 cells, 7–8 slices, 7–8 mice.

Figure 3: DA mobilizes astrocytic Ca^{2+} in PFC slices via cell-surface ARs. (A) Schematic for 2P astrocytic Ca^{2+} imaging in acute slices. **(B)** Representative micrograph of GCaMP6f expression in imaged

PFC area. Note y-axis measurements of distance to slice midline, used for spatial plots in (D). **(C)** All AQuA-detected Ca^{2+} events 0–60s before (left) and 90–150s after DA bath-application (right) from same slice as in (B). Colors represent individual events. **(D)** Time-course of all Ca^{2+} events detected over entire recording of slice in (B–C) and event onset rate (top) relative to 10μM DA (t=0). Shaded areas represent approximate event size and mean event y-position over time. **(E)** Astrocytic Ca^{2+}-event rate (count/5s) in PFC slices after treatment with indicated drugs. Treatment with both D1 and D2 agonists SKF38393 and Quinpirole (yellow) did not induce increased Ca^{2+} events as DA did (magenta). Blocking both D1R and D2R with antagonists SCH23390 and Sulpiride during DA application (blue) failed to occlude astrocyte activation by DA, whereas the effect of DA alone was reduced in $IP_3R2^{-/-}$ mice (grey). Non-selective α- and β-AR antagonists Phentolamine and Propranolol (green) reduced Ca^{2+} responses to DA. Slices (transparent dots) and corresponding mean±sem (solid dot and error bar): 48.0±10.2 (DA); 8.0±2.5 (D1/D2 ago.); 23.6±4.6 (DR antag.); 9.9±3.3 ($IP_3R2^{-/-}$); 9.3±2.5 (AR antag.). Kruskal-Wallis test after Levene test; *, $p<0.05$ compared to DA condition; all other comparisons between conditions (not shown), $p>0.79$; n=5–8 slices, 4–8 mice. **(F)** Example of tissue-wide expression of $GRAB_{NE}$ in acute slice. **(G)** DA is not metabolized to NE in PFC slices, as indicated by $GRAB_{NE}$. Left: trace means±sem relative to either DA or NE addition at t=0. Right: slices (dots) and mean±sem (dot with error bar) of 20-s $GRAB_{NE}$ dF/F averages at baseline (black), or 6 min after 10μM DA (magenta) and 10μM NE (grey): -0.002±0.003 (Baseline); 0.055±0.012 (DA); 1.490±0.165 (NE). Kruskal-Wallis test after Levene test; ***, $p<0.001$ relative to baseline; n=6 slices, 4 mice. **(H)** Example slice from $OCT3^{-/-}$ mice with deficient DA uptake, loaded with the Ca^{2+} indicator Fluo-4. **(I)** Somatic Ca^{2+} signals in response to bath-applied DA are present in PFC astrocytes in the $OCT3^{-/-}$ background. Left: mean trace (black) and slice average traces of active cells (grey) relative to 10μM DA addition at t=0. Right: slice averages (lines) and corresponding mean±sem (dots and error bars) of Fluo-4 dF/F extracted from traces on left at either 100-s before (Basal) or after DA (+DA): -0.04±0.02 (Baseline); 0.22±0.08 (+DA). Paired t-test after Anderson-Darling test; *, $p<0.05$; n=138 active cells, 6 slices, 3 mice.

Figure 4: Photo-uncaging releases physiological concentrations of DA and activates astrocyte territories in seconds. (A) Schematic for fast release of DA in PFC slices using RuBi-DA uncaging with a blue LED, combined with simultaneous 2P imaging of DA (dLight1.2) or astrocytic Ca^{2+} (GCaMP6f). **(B)** Representative dLight expression an acute PFC slice. **(C)** dLight dose-response to DA in PFC slices and Hill equation fit function (solid line). Dotted lines indicate DA concentration at dLight half-maximum. Slices mean±sem (dots and error bars); n=4 slices, 2 mice. **(D)** dLight fluorescence (dF/F) increases after LED stimulation (3x100-ms pulses, blue line) in presence of RuBi-DA (magenta) but not in control without RuBi-DA in bath (grey). Trace mean±sem; n=6–7 slices, 3 mice. **(E)** Estimated DA concentration post-uncaging was 2μM, extrapolated from fit function in (C) using data from (D) obtained as 30-s dF/F means after LED stimulus. All slices (transparent dots) and corresponding mean±sem (solid dot and error bar): 0.41±0.03 (Control), 2.0±0.2 (RuBi-DA) μM. Two-sample t-test, ***, $p<10^{-6}$; n=6–7 slices, 3 mice. **(F)** Representative PFC slice for 2P imaging of astrocytic GCaMP (top) with corresponding astrocyte territories (bottom). **(G)** Raster-plots of AQuA-detected Ca^{2+} events (top) show time-course of events within cells from slice in (F), plotted relative to LED (blue lines, t=0) before (left, control) and after bathing on RuBi-DA (right). Colors indicate co-occurring event number/cell. Bottom graphs: cumulative event counts across cells. **(H)** Ca^{2+} activity increases for majority of cells in 60s after uncaging (70%), while cells are largely inactive (no events throughout recording; 91%) in the control condition. Percent of cells decreasing or maintaining their activity after uncaging is similar between conditions. Mean±sem; n=540–1118 cells, 5–11 slices, 5–8 mice. % Cells (Control, RuBi-DA): 91±2, 30±7 (Inactive); 4±1, 62±8 (Increase); 4±1, 4±1 (Decrease); 0±0, 4±1 (No change). **(I)** Ca^{2+} event features (number, area, duration) in active cells in (H) increase significantly in the 60s after uncaging (blue boxes) with RuBi-DA (magenta) but not without (control, black). Slice averages of active cells (grey lines) and mean±sem (dots and error bars). Event # (pre-, post-uncaging): 0.06±0.02, 0.07±0.01 (Control); 0.17±0.03, 1.22±0.16 (RuBi-DA). Event area (μm^2): 25±7, 23±3 (Control); 20±5, 443±104 (RuBi-DA).

Event duration (s): 3.0±0.7, 2.7±0.2 (Control); 1.9±0.8, 11.3±1.5 (RuBi-DA). Paired t-test comparing pre- to post-uncaging; **, $p<0.01$; ***, $p<0.001$. Control: n=47/540 active/total cells, 5 slices and mice. RuBi-DA: n=784/1118 cells, 11 slices, 8 mice. **(J)** Example of Ca^{2+} activation within cells 5s after uncaging pulse, either in control (left) or with RuBi-DA (right). Maps are zoomed in from (F). Grey=cell areas; magenta=active pixels. **(K)** Time-course of % cell area active relative to uncaging (blue lines) in absence and presence of RuBi-DA. Cells, slices, and overall mean (grey, thin and thick colored lines, respectively). Control: n=47/540 cells, 5 slices and mice. RuBi-DA: n=784/1118 cells, 11 slices, 8 mice. **(L)** Response to DA (magenta) occurs within seconds (left, delay), lasts <20s (middle, peak full-width half-maximum), and recruits areas within individual astrocytes (right, % cell surface). In controls (black), few cells were active post-uncaging, with short activity (< 9s) covering a small percentage of cell area. Control: n=22 cells, 5 slices, 5 mice. RuBi-DA: n=720 cells, 11 slices, 8 mice.

Figure 5: Fast astrocyte responses to DA in PFC slices occur via α1-ARs. (A) Schematic for RuBi-DA uncaging and simultaneous 2P Ca^{2+} imaging in PFC slices bathed with receptor antagonists. **(B)** Ca^{2+} increases shortly after RuBi-DA uncaging (control), an effect blocked by α1-AR antagonist Doxazosin (10μM), but not by D1 (SCH23390, 10μM), D2 (Sulpiride, 0.5μM), α2-AR (Idazoxan, 10μM) or β-AR (Propranolol, 10μM) antagonists. Data relative to uncaging (blue lines, t=0) as slice average traces (grey lines) of AQuA-detected, z-scored Ca^{2+} events in GCaMP6f-expressing astrocytes, with overall mean as colored traces. **(C)** Quantification of (B), shown as 30-s mean of slice Ca^{2+} immediately before (white) or after RuBi-DA uncaging (blue) in presence of inhibitors. Slices (grey lines) and corresponding mean±sem (black lines, solid dots, and error bars): 0.03±0.10, 1.08±0.17 (control); 0.07±0.07, 0.83±0.06 (D1); 0.02±0.10, 1.21±0.20 (D2); 0.39±0.10, 0.47±0.09 (α1); -0.03±0.06, 0.82±0.15 (α2); 0.19±0.12, 1.09±0.21 (β). Paired t-test after Anderson-Darling test to compare pre- to post-uncaging values; *, $p<0.05$, **, $p<0.01$; $p=0.004$ (control), 0.0006 (D1), 0.008 (D2), 0.624 (α1), 0.008 (α2), 0.036 (β); n=6–9 slices, 5–9 mice. Pre-uncaging values in treatments versus control were not statistically different (Kruskal-Wallis test with Dunn's correction: adjusted p-value >0.19 for all comparisons).

Figure 6: Astrocyte Ca^{2+} follows DA release *in vivo* via α1-ARs. (A) Left: Schematic for dual-color FP in PFC of behaving mice for DA (dLight1.2, green) and astrocyte Ca^{2+} (jR-GECO1b, magenta). Right: example traces during aversive tail lift (triangles). **(B)** Average FP traces for DA and Ca^{2+} in PFC, aligned to Ca^{2+} transient onsets. Mean±sem; n=96 transients, 9 mice. **(C)** Response amplitude for DA (green) and Ca^{2+} (magenta) in aversive stimulation experiments deviate from baseline values (dLight: 0.89±0.04 dF/F; jR-GECO: 0.31±0.04 dF/F). Tukey boxplots, calculated as maximum dF/F relative to 20-s mean before the jR-GECO peak. One-sample t-test or sign test with hypothesized mean 0, after Anderson-Darling test to show difference from 0; ***, $p<0.001$; n=96 transients, 9 mice. **(D)** Cross-correlation of dLight and jR-GECO traces (left) indicates that DA signals *in vivo* precede Ca^{2+} transients by 1.4±0.2 s (right). Mean±sem and Tukey boxplots; one-sample sign test with hypothesized mean 0, ***, $p<0.001$; n=96 transients, 9 mice. **(E)** Schematic of dual-color FP in PFC of mice treated with the LC-toxin DSP4 (50mg/kg, i.p., 2 injections, 2 days apart), before and after administration of α1-AR antagonist Prazosin (5mg/kg, i.p.). **(F)** LC inputs to PFC revealed by NET staining (top, naïve) are decreased after DSP4 (bottom). **(G)** In NE-depleted animals, DA transients (left, dLight) during aversive stimulation in PFC are still present (DSP4, orange; 1.02±0.11 dF/F) and unaffected when α1-ARs are blocked (+ Prazosin, aqua; 0.77±0.05), whereas Ca^{2+} peaks (right, jR-GECO) are significantly reduced by Prazosin (DSP4: 0.11±0.01 dF/F; +Prazosin: 0.04±0.0 dF/F), indicating that PFC Ca^{2+} relies on α1-ARs even with diminished NE. Tukey boxplots, calculated as maximum dF/F relative to 20-s means before jR-GECO peaks. Wilcoxon rank sum test; ***, $p=0.0003$; n=27–29 transients, 4 mice. **(H)** Cross-correlation of dLight and jR-GECO traces (left) in NE-depleted animals (DSP4), and in the same animals after inhibition of α1-ARs (DSP4 + Prazosin) shows that DA signals in PFC precede Ca^{2+} with diminished NE (DSP4, -2.64±0.52 s) but not after inhibition of α1-ARs (+Prazosin, 0.73±0.65 s). Trace mean±sem and Tukey boxplots; Wilcoxon rank sum test; ***, $p=0.0003$; n=27–29 transients, 4 mice.

Figure 7: DA mobilizes ATP at discrete locations at PFC astrocytes via α1-ARs. (A) Schematic for 2P astrocytic $GRAB_{ATP}$ imaging in acute PFC slices. **(B–C)** Continuous bath-application of ATP (50μM) induces strong, sustained fluorescent signals in astrocytes, shown as (B) PFC astrocytes expressing $GRAB_{ATP}$ (grayscale) with color overlay of AQuA-detected ATP events before (left, basal) and after ATP (right), and (C) time course of the dF/F amplitude of AQuA-detected ATP events relative to exogenous ATP application (t=0). Mean±sem of slice traces n=52/62 active/total cells, 8 slices, 3 mice. **(D)** $GRAB_{ATP}$ event rate increases following ATP stimulation. Slice averages (lines) and mean±sem (dots and error bars): 0.0007±0.0007 (Basal), 0.010±0.001 (+ATP) min^{-1}. Paired t-test after Anderson-Darling test; ***, $p<10^{-4}$; n=8 slices, 3 mice. **(E)** $GRAB_{ATP}$ events in response to continuous ATP application covered the entire astrocyte territory (left, 1044±224 μm^2) and were sustained (right, 100±16s). Slice averages of active cells (transparent dots) and overall mean±sem (solid dots and error bars); n=8 slices, 3 mice. **(F–H)** Application of DA (10μM) (F) induces localized ATP events, shown as (G) $GRAB_{ATP}$ micrographs and AQuA overlay, which are delayed (H) relative to DA application (t=0). Mean±sem of slice averages n=23/101 active/total cells, 10 slices, 5 mice. **(I)** ATP event rate after DA application was higher than baseline. Slice averages (lines) and mean±sem (dots and error bars): 0.0007±0.0004 (Basal), 0.005±0.001 (+DA) min^{-1}. Paired t-test after Anderson-Darling test; *, p=0.025; n=10 slices, 5 mice. **(J)** $GRAB_{ATP}$ events in response to DA were smaller than entire astrocyte territories (221±52μm^2) and time-restricted (30±8s). Slice averages of active cells (transparent dots) and overall mean±sem (solid dots and error bars); n=9 slices, 5 mice. **(K–M)** In presence of α1-AR antagonist Doxazosin (10 μM), DA (K) does not induce ATP events, as shown by (L) $GRAB_{ATP}$ micrographs and AQuA overlay, and (M) time-course of $GRAB_{ATP}$ event dF/F relative to DA application (t=0, 10μM). Mean±sem of slice averages (line and shaded area). n=41/160 active/total cells, 10 slices, 5 mice. **(N)** In presence of Doxazosin, DA application does not increase ATP event rate. Slice averages (lines) and mean±sem (dots and error bars): 0.0028±0.0008 (Basal), 0.0026±0.0005 (+Dox/+DA) min^{-1}. Paired t-test after Anderson-Darling test; n.s., p=0.878; n=10 slices, 5 mice. **(O)** $GRAB_{ATP}$ events in presence of Doxazosin are similar in size (267±53μm^2) and duration (48±20s) to those observed in DA alone. Slice averages of active cells (transparent dots) and overall mean±sem (solid dots and error bars); n=10 slices, 5 mice.

STAR★Methods

Resource availability

Lead contact

Further information and requests for resources and reagents may be directed to and will be fulfilled by the lead contact, Dr. Kira Poskanzer (kira.poskanzer@ucsf.edu).

Materials availability

This study did not generate new reagents.

Data and code availability

- All data reported in this paper will be shared by the lead contact upon request.
- This paper does not report original code.
- Any additional information required to reanalyze the data reported in this paper is available from the lead contact upon request.

Experimental model and subject details

Animals

Experiments were carried out as detailed below, using young adult for *ex vivo* (P27–54) or adult mice (P50–130) for *in vivo* experiments, in accordance with protocols approved by the University of California, San Francisco Institutional Animal Care and Use Committee (IACUC). Animals were housed in a 12:12 light-dark cycle with food and water provided *ad libitum*. Male and female mice were used whenever available. For *in vivo* experiments following surgery, all animals were singly housed to protect implants and given additional enrichment. Animals were included when sensor expression was sufficient to visualize sensor dynamics; animals were excluded from uncaging experiments when no response to dopamine uncaging was detected upon a test uncaging stimulus. Transgenic mice used in this study were Lck-GCaMP6f$^{fl/fl}$ mice (Srinivasan et al., 2016) and *Aldh1l1*-Cre/ERT2 mice (Srinivasan et al., 2016) from the Khakh lab (UCLA, USA), *Drd1a*-tdTomato (Shuen et al., 2008) and *Drd2*-EGFP (Gong et al., 2003) from the Bender lab (UCSF, USA), *Aldh1l1*-EGFP and *Aldh1l1*-tdTomato (Gong et al., 2003) from JAX (USA), *Itpr2*-deficient mice ($IP_3R2^{-/-}$) (Li et al., 2005) from Dr. Katsuhiko Mikoshiba (RIKEN, Japan) and *Slc22a3*-deficient mice ($OCT3^{-/-}$) (Zwart et al., 2001) from the Irannejad lab (UCSF, USA).

Method details

Surgical procedures

For viral expression in *ex vivo* experiments, neonatal mice (P0–4) on C57Bl/6 or Swiss background were anesthetized on ice for 2 min before injecting viral vectors (*AAV5-GfaABC$_1$D-GCaMP6f* [1.4–5.42e^{13}; all titers in GC/ml], *AAV9-hGfap-pinkFlamindo* [6.6e^{13}], *AAV9-hSyn-NE2.1* [5.72e^{13}], *AAV9-CAG-dLight1.2* [9.5e^{15}], or *AAV9-hSyn-ATP1.0* [4.89e^{13}]). Pups were placed on a digital stereotax and coordinates were zeroed at the middle point along the line connecting the eyeballs. Two injection sites over PFC were chosen at 0.25–0.34 mm lateral, and 1 and 1.4 mm caudal. At each injection site, 30–100nl of virus were injected at a rate of 3–5nl/s at two depths (0.7–0.85, and 0.9–1 mm ventral) using a microsyringe pump (UMP-3, World Precision Instruments).

For *in vivo* 2P imaging, we expressed Lck-GCaMP in astrocytes of adult mice (P50–130), either by crossing Lck-GCaMP6f$^{fl/fl}$ mice to *Aldh1l1*-Cre/ERT2 (Srinivasan et al., 2016) and treating them with tamoxifen (0.1mg/kg, i.p., for 5 consecutive days, 4–6 weeks before imaging), or via viral vectors (see below) in C57Bl/6 mice. For FP, we expressed dLight and astrocytic jR-GECO1b via viral vectors (see below) in C57Bl/6 mice (P60–90). Before surgical procedures, adult mice were administered dexamethasone (5mg/kg, s.c.) and anesthetized with isoflurane, and a 1- or 3-mm diameter craniotomy was created over PFC (+1.7–1.8 mm rostral, +0.5 mm lateral from Bregma) or visual cortex (-3.5mm caudal, +1.2 mm lateral from Bregma). Viral vectors (*AAV5-GfaABC$_1$D -Lck-GCaMP6f-SV40* [1.4–5.42e^{13}], *AAV5-hSyn-dLight1.2* [4e^{12}], *AAV9-GfaABC$_1$D-Lck-jRGECO1b* [2.24e^{14}]) were delivered using a microsyringe pump (100–600 nl, 30–60 nl/min) before implanting optical devices. For 2P imaging in PFC, after careful removal of meninges, a GRIN lens (1-mm diameter, 4.38-mm length, WDA 100, 860 nm, Inscopix) was slowly lowered to -2.4mm ventral; for 2P imaging in V1, a cranial window was placed above the tissue; a custom-made titanium headplate was then attached to the skull. For FP in PFC, a fiber optic cannula (Mono Fiberoptic Cannula, 400μm core, 430nm, 0.48 NA, 2.8mm length, Doric Lenses) was implanted at the same depth as GRIN lenses. All imaging devices were secured in place using dental cement (C&B Metabond, Parkell). Post-operative care included administration of 0.05mg/kg buprenorphine and 5mg/kg carprofen. Mice were allowed a minimum of 14 days to recover, then habituated to head-fixation on a circular treadmill or to fiber optic coupling in a freely moving arena prior to experiments.

In vivo 2P imaging and locomotion

2P imaging experiments were carried out on an upright microscope (Bruker Ultima IV) equipped with a Ti:Sa laser (MaiTai, SpectraPhysics). The laser beam intensity was modulated using a Pockels cell

(Conoptics) and scanned with linear galvanometers. Images were acquired with a 16×, 0.8 N.A. (Nikon) or a 20×, 1.0 N.A. (XLUMPLFLN-W, Olympus) water-immersion objective via photomultiplier tubes (Hamamatsu) using PrairieView (Bruker) software. For GCaMP imaging, 950 nm excitation and a 515/30 emission filter were used. Mice were head-fixed on a circular treadmill and Ca^{2+} activity was recorded at ~1.7 Hz frame rate from putative PFC or V1 cortex, at 512×512 pixels and ~0.6μm/px resolution. Locomotion speed was monitored using an optoswitch (50mA, 2V; OPB800L55, TT Electronics, Newark) connected to a microcontroller board (Arduino Uno R3, Arduino) and acquired at 1KHz simultaneously with 2P imaging using PrairieView.

Ex vivo 2P imaging and uncaging

Coronal, acute PFC slices (300-μm thick) from P27–54 mice were cut with a vibratome (VT 1200, Leica) in ice-cold cutting solution containing (in mM) 27 $NaHCO_3$, 1.5 NaH_2PO_4, 222 sucrose, 2.6 KCl, 2 $MgSO_4$, 2 $CaCl_2$. Slices were transferred to pre-heated, continuously aerated (95% O_2/5% CO_2) standard artificial cerebrospinal fluid (ACSF) containing (in mM) 123 NaCl, 26 $NaHCO_3$, 1 NaH_2PO_4, 10 dextrose, 3 KCl, 2 $MgSO_4$, 2 $CaCl_2$. Younger mice were sliced in the same solutions for dLight (P18–28) and $GRAB_{NE}$ (P24–35) experiments, and one P19 $IP_3R2^{-/-}$ experiment (otherwise P31–36). Slices were kept at room temperature until imaging, and experiments performed at 37°C. To block neuronal action potentials and neuron-to-astrocyte-communication during imaging, at least 10 min before experiments recirculating standard ACSF was switched to a multi-drug cocktail mix, containing (in μM) 1 TTX, 100 LY341495, 1 CGP 55845, 2 AM251, 1 CGS 15943, 100 PPADS, 5 Ipratropium, unless otherwise stated.

Slice recordings were done in coronal sections above medial prefrontal cortex, and the imaging area was ~ 0.6–0.8 mm x 0.8 mm over prelimbic and infralimbic areas, with the top part of the imaging area corresponding to the midline, thus spanning all cortical layers. Images were acquired from putative PL-IL cortex in PFC slices at a minimum depth of 50 μm, using the same setup as for *in vivo* 2P imaging or a custom-made upright microscope and ScanImage software, at 1.42–1.53 Hz frame rate, 512×512 pixels and 1.04–1.61 μm/px resolution. Fluorophores were excited at (in nm) 950–980 (GCaMP), 1040 (Pink Flamindo), 980 (dLight), 920 ($GRAB_{NE}$ and $GRAB_{ATP}$). Emission was collected with a 515/30 or 525/50 filter for green and a 605/15 or 600/40 filter for red fluorophores. For bath-application experiments, a 5-min baseline was recorded to monitor spontaneous activity, after which neuromodulators were added along with a fluorescent dye (AlexaFluor 594 Hydrazide) to assess the time at which drugs reached the imaging field (except for Pink Flamindo due to spectral overlap).

For RuBi-DA uncaging, a fiber optic cannula (400-μm core, 0.39 NA; CFM14L10, ThorLabs) was coupled to a compatible fiber optic (M79L005, ThorLabs) and a blue LED (470 nm; M470F3, ThorLabs), and placed adjacent to the imaging field using a micromanipulator (MX160R, Siskiyou). Illumination (3

pulses, 100-ms duration, 50-ms intervals) was triggered using the imaging software (PrairieView, Bruker) connected to the LED-driver cube (LEDD1B, ThorLabs). Light power was 2–4 mW.

For pharmacology experiments in Figure 2, we note that Quinpirole is a full agonist at all D2-like DRs (D_2, D_3 and D_4). However, because all D2-like receptors are coupled to G_s proteins—thus canonically linked to increases in cAMP levels—we assumed that this widely used D2 agonist would cause similar changes in cAMP regardless of the receptor subtype. Likewise, SKF81297 is a full agonist at all D1-like receptors (D_1 and D_5). Because no response to D1R/D2R stimulation was detected, we did not explore the contribution of individual receptor subtypes further.

Fiber photometry recordings

FP experiments were carried out using an RZ10 FP processor equipped with Lux integrated 405, 465, and 560-nm LEDs and photosensors (Tucker-Davis Technologies). Animals implanted for FP were placed in a freely moving arena in which the mouse was able to move in all directions, after coupling to low autofluorescence fiberoptic patchcords (400-µm core, 0.57 NA; Doric Lenses) connected to photosensors through a rotary joint (Doric Lenses). FP fluorescence signals were recorded for 10 minutes, during which tail lifts were performed every minute. For a tail lift stimulation, the experimenter held and lifted the tail of the animal until its hind paws disconnected from the ground; after that the tail was released. With this experimental paradigm, no pain or harm is caused to the animal. After baseline recordings, animals were treated with DSP4 (50 mg/kg, i.p., 2 injections 2 days apart) and recorded again 4 days after the first DSP4 administration. Following DSP4 recordings, animals were injected with Prazosin (5 mg/kg, i.p.) and recorded again 20 minutes later.

Immunohistochemistry

Mice were intracardially perfused with 4% PFA, brains were then collected, immersed in 4% PFA overnight at 4°C and switched to 30% sucrose for two days before being frozen on dry ice and stored at -80°C. Brains were sliced coronally (40-µm thick) on a cryostat, and slices stored in cryoprotectant at -20°C until staining. Slices were washed 3x in PBS for 5 min, then permeabilized for 30 min with 0.01% TritonX in PBS. Slices were next washed with 10% NGS (Invitrogen) for 1 h and incubated overnight with primary antibodies at 4°C in 2% NGS. Slices were next rinsed 3x in PBS before incubating for 2 h at room temperature with secondary antibodies, then washed 3x in PBS for 5 min before slide-mounting and coverslipping using Fluoromount with DAPI. To stain for EGFP and tdTomato in D1, D2 and Aldh1l1 colocalization experiments, primary antibodies used were rat anti-mCherry (1:1000, Thermo Fisher Scientific) and chicken anti-GFP (1:3000, Aves Lab) in 2% NGS. Secondary antibodies used were goat anti-rat Alexa Fluor 555 (1:1000) and goat anti-chicken Alexa Fluor 488 (1:1000). To stain brain tissue

from GRIN lens experiments, primary antibodies used were rat anti-GFAP (1:1000, Thermo Fisher Scientific) and chicken anti-GFP (1:3000, Aves Lab) for Lck-GCaMP. To stain for dLight and jR-GECO1b in sections from FP experiments, primary antibodies used were rat anti-mCherry (1:1000, Thermo Fisher Scientific) and chicken anti-GFP (1:3000, Abcam). Secondary antibodies used were goat anti-rat Alexa Fluor 555 (1:1000, Thermo Fisher Scientific) and goat anti-chicken Alexa Fluor 488 (1:1000, Thermo Fisher Scientific). For NET staining, sections were incubated for 1 h with a secondary mouse block (AffiniPure Fab Fragment IgG, 30 µg/ml, Jackson ImmunoResearch) before primary antibody mouse anti-NET (1:100, MAb Technologies), and secondary antibody goat anti-mouse Alexa Fluor 555 (1:1000, Thermo Fisher Scientific). Z-stacks or whole-brain images were acquired at 40x or 2x using a Keyence BZ-X800 fluorescence microscope and stitched with Keyence Analysis Software.

Quantification and statistical analysis

Colocalization cell counts

To estimate colocalization, 3 slices/mouse were chosen at +1.8, +1.7 and +1.6 mm from bregma, and tiled z-stack images were acquired on a spinning disk confocal (Zeiss) at PFC spanning cortical layers 1–6. Colocalization counts of $tdTomato^+$ and $EGFP^+$ cells were performed using Cell Counter in Fiji (ImageJ).

2P image and data analysis

When necessary, videos were preprocessed by registering images using the ImageJ plugin MoCo (Dubbs et al., 2016). Cell maps for Pink Flamindo, $GRAB_{ATP}$, and uncaging experiments were drawn using the interactive wand segmentation tool (SCF-MPI-CBG plugin).

AQuA event detection

Ca^{2+} and ATP 2P image sequences were analyzed using AQuA software (Wang et al., 2019) and custom MATLAB (Mathworks) code. Signal detection thresholds were adjusted for each video to account for differences in noise levels after manually checking for accurate AQuA-detection. Events were thresholded post-detection at 25 μm^2 and 2 s for *ex vivo*, or 50 μm^2 and 2 s for *in vivo* Ca^{2+} imaging, and at 50 μm^2 and 2.5 s for $GRAB_{ATP}$ imaging. Event count was quantified using the onset of each event as detected by AQuA. Area is defined as the footprint occupied by an event over its entire lifetime. Number of co-occurring events is calculated as the number of events co-existing temporally anywhere in the imaging field with a given event. Number of co-localized events is calculated as the number of events having comparable size (0.5–2x) and overlapping spatially with a given event.

In vivo *2P imaging and locomotion analysis*

For locomotion-aligned astrocyte Ca^{2+} analysis, only locomotion bouts longer than 2s and starting more than 10s after the previous locomotion bout ended were considered (Fig S1H). Population-wide mean Ca^{2+} traces (Fig 1I) were obtained by normalizing the fluorescence of each AQuA-detected event as $(F-F_{min})/(F_{max}-F_{min})$ and then averaging across events. For max Ca^{2+} (Fig 1K), changes in normalized fluorescence were thresholded at 0.1 to exclude noise. For astrocyte Ca^{2+}-aligned locomotion analysis (Fig 1L), astrocyte Ca^{2+} event dF/F was used and all locomotion bouts were considered. Locomotion speed was calculated as cm/s.

Bath-applied DA analysis

For bathed-DA experiments, Ca^{2+} event rate was calculated as counts of AQuA-event onsets in 5-s bins (Ca^{2+}), and events for the post-treatment condition (Fig 3E) were analyzed over a 30-s window centered at 90-s post drug or at the timepoint when the event rate exceeds baseline (6 STD of event rate at baseline). We then calculated the peak onset as the last local minimum before the peak, and—to overcome false positives due to noise—we constrained the local minima to be below the 6 STD threshold for peak detection. At baseline (Fig S3B) we used a 60-s window to account for low number of spontaneous events. For $GRAB_{ATP}$, events were analyzed over 300-s windows, immediately before (basal) and 90-s post drug. The 300-s window (for the post-drug condition) was started 90-s after the delivery of the drug since we wanted to probe ATP events that would follow DA-induced Ca^{2+} events, which—in bath application experiments (Fig. 3)—started ~90s after drug delivery.

Single-cell ex vivo *uncaging analysis*

Classification of cell activity around uncaging was done based on counts of AQuA-event onsets in the 60-s before versus 60-s after uncaging (t=0). Event features (count, area, duration) were averaged by cell and slice using the same temporal windows. Traces for the % of cell area active were obtained as the overall number of pixels/frame occupied by AQuA-detected events within an individual astrocyte (cell territories were defined by cell maps, see above). Traces were analyzed with custom-written code in MATLAB to find peak times, amplitudes (max % cell surface active) and duration (FWHM). Latency to peak onset after uncaging (delay) was obtained as the first timepoint above threshold (6 STD of the pre-uncaging activity).

ROI-based analysis

Pink Flamindo, $GRAB_{NE}$ and dLight videos were analyzed using ROI-based approaches in ImageJ. Changes in fluorescence intensity were calculated as $(F-F_0)/F_0$ (dF/F), where F_0 is the average intensity of the first 20–30 frames. For $GRAB_{NE}$, dF/F values were extracted as 20-s means at 50 s before (pre-drug)

or 340 s after compound addition. Fluo-4 videos from OCT3 KO experiments were analyzed using CalTracer 3 Beta (Poskanzer and Yuste, 2016), dF/F traces extracted from the automatically detected cell somata, and identified peaks checked manually for accurate detection before extracting duration and latency. Traces' dF/Fs were then obtained as 5-s means at 100 s before or after DA addition based on average peak latencies. Data for the dLight dose-response curves were fit to a Hill equation (y = a + (b-a)/(1+10^((c-x)*d))), and DA concentrations released by RuBi-DA uncaging were extrapolated from the obtained fit function based on changes in dLight fluorescence after uncaging.

Pink Flamindo analysis

For Pink Flamindo experiments, background fluorescence was subtracted from raw fluorescence traces. To identify steady-state increases or decreases in fluorescence, traces were smoothened using a moving average and then fit using a modified Boltzmann's sigmoidal equation y=a+(b-a)/(1+exp((c-x)/d), where a is the bottom, b is the top, c is the inflection point and d is the slope, using a nonlinear least squares algorithm (Levenberg-Marquardt) in MATLAB. Fit constraints were (b-a)>noise, slope<10, and inflection point at x>0. Cells where the sigmoid fit of the trace in response to Forskolin did not converge were excluded from all previous analyses. Cells with high noise (>0.1 dF/F) or drift (when change in dF/F before drug application exceeded noise) were removed. Noise was calculated as 3 STD at baseline. Average dF/F values (Fig 2G) were then extracted as 20-s means at 40 s before (control) or 240 s after compound addition (drug/Forskolin) from original traces.

Fiber photometry analysis

FP data were preprocessed by downsampling and subtraction of the isosbestic channel linear fit (as in https://www.tdt.com/docs/sdk/offline-data-analysis/offline-data-python/FibPhoEpocAveraging), detrended to correct bleaching, and dF/F calculated as above (F_0 obtained at 0–15 s). Traces were then denoised using an IIR lowpass filter in MATLAB (cutoff frequency 1Hz, steepness 0.95). Transients in jR-GECO1b traces were detected using the 'findpeaks' function in MATLAB (applied over normalized traces, with minimum peak height and prominence set to 25% and at a minimum distance of 20 s, according to the timing of the tail lift stimulation protocol. All trials/animals were analyzed using the same parameters for peak detection.) Transient onsets were determined as the timepoints where the first derivative exceeded 1 STD. Then, dLight and jR-GECO1b traces were extracted in 40-s windows centered at onsets, and the cross-correlation function calculated from the extracted traces with a 6-s maximum lag to obtain the latency to maximum cross-correlation. Response amplitudes (Fig 6C,G) were calculated for each detected peak as change in dF/F between trace average before onset and trace maximum after onset.

Statistics

Statistics used for each dataset and their results, as well as the exact value of n and whether n represents cells, animals or replicates, and the definition of center, dispersion and precision are detailed in the figure legends. To compare one group of data with a hypothesized mean value we used a one-sample t-test or sign test (Wilcoxon) as appropriate after a normality test. When comparing two unpaired groups, we used the two-sample, unpaired t-test or the Wilcoxon rank sum test (Mann-Whitney) as appropriate after a normality test. When comparing two paired groups of data, we used the paired t-test or the Wilcoxon signed rank test after checking for normality on the difference between groups. Normality was checked using the Anderson-Darling test. When comparing treatments for three or more groups (Fig 3E,G) we used one-way Anova or the Kruskal-Wallis test after testing for equal variances using the Levene test (quadratic). For Pink Flamindo data (Fig 2G), we used the non-parametric Friedman test for paired data after the Levene test to compare within conditions (control, drug, Forskolin), and one-way Anova or Kruskal-Wallis test after the Levene test to compare across treatments. Multiple comparisons in Fig. 5 were not corrected *post hoc* to minimize type II errors (i.e., to avoid increasing the rate of false negatives; in a false negative, pre- to post-uncaging values would be erroneously considered non-significantly different from each other). All statistical tests are two-tailed unless otherwise stated in the figure legend (Fig. S5B).

Statistical significance for time-series data was computed using the shuffle test with custom-written code in MATLAB. Data pairs were selected as a reference value (trace mean from $t<0$ or the entire time window analyzed) and a given timepoint in the time-series ($t>0$ or all timepoints in the window). Data from the two groups were pair-wise shuffled for 10000 repetitions to calculate the difference between the two populations, the significance level α for rejecting H_0 was set to 0.01, and Bonferroni correction was applied to account for multiple comparisons.

Supplemental Videos

Video 1, related to Fig 1: PFC astrocytes *in vivo* display cell-restricted Ca^{2+} activity unlinked to animal locomotion.

Ca^{2+} events in PFC (left) and V1 (right) astrocytes, with their relationship to animal locomotion. Top: raw Lck-GCaMP6f videos with overlaid AQuA-detected Ca^{2+} events (colors are individual events). Bottom: time course of astrocyte activity shown as population-level Ca^{2+} traces with corresponding animal locomotion speed below. Images acquired at 2Hz, playback speed 15fps.

Video 2, related to Fig 3: Robust astrocyte Ca^{2+} response to DA stimulation of PFC slices.

Bath-application of DA (10μM) in PFC slices expressing GCaMP6f in astrocytes induces a robust, but delayed Ca^{2+} mobilization. Neuronal action potentials and neuron-to-astrocyte communication are blocked with TTX and a drug cocktail (see Methods). Top: raw video; bottom: AQuA-detected Ca^{2+} events. Time stamps relative to DA application.

Video 3, related to Fig 4: DA uncaging induces fast, transient Ca^{2+} activation in PFC astrocytes.

RuBi-DA (right) uncaged at t=0 on GCaMP6f-expressing astrocytes in a PFC slice, inducing a robust Ca^{2+} response within seconds. In the same slice, the light stimulation protocol in the absence of RuBi-DA (control, left) has no effect. Top: raw videos; bottom: overlaid AQuA-detected Ca^{2+} events (colors are individual events). Time indicated in seconds from uncaging.

Video 4, related to Fig 5: DA acts on PFC astrocytes via α1-ARs.

Representative experiments in PFC slices expressing GCaMP6f in astrocytes, in which RuBi-DA is uncaged at t=0s in presence of different DR and AR antagonists. Labels indicate drugs (Control: no antagonist; D1: SCH23390 10μM; D2: Sulpiride 0.5μM; α1: Doxazosin 10μM; α2: Idazoxan 10μM; β: Propranolol 10μM). Uncaging light pulses appear as white stripes due to detector saturation. Only Doxazosin application blocks uncaging-induced astrocyte activation.

References

Abbink, M.R., van Deijk, A.-L.F., Heine, V.M., Verheijen, M.H., and Korosi, A. (2019). The involvement of astrocytes in early-life adversity induced programming of the brain. Glia *67*, 1637–1653.

Abercrombie, E.D., Keefe, K.A., DiFrischia, D.S., and Zigmond, M.J. (1989). Differential effect of stress on in vivo dopamine release in striatum, nucleus accumbens, and medial frontal cortex. J. Neurochem. *52*, 1655–1658.

Agnati, L.F., Zoli, M., Strömberg, I., and Fuxe, K. (1995). Intercellular communication in the brain: wiring versus volume transmission. Neuroscience *69*, 711–726.

Alachkar, A., Brotchie, J.M., and Jones, O.T. (2010). Binding of dopamine and 3-methoxytyramine as l-DOPA metabolites to human alpha(2)-adrenergic and dopaminergic receptors. Neurosci. Res. *67*, 245–249.

Amphoux, A., Vialou, V., Drescher, E., Brüss, M., Mannoury La Cour, C., Rochat, C., Millan, M.J., Giros, B., Bönisch, H., and Gautron, S. (2006). Differential pharmacological in vitro properties of organic cation transporters and regional distribution in rat brain. Neuropharmacology *50*, 941–952.

Anastasiades, P.G., Boada, C., and Carter, A.G. (2019). Cell-Type-Specific D1 Dopamine Receptor Modulation of Projection Neurons and Interneurons in the Prefrontal Cortex. Cereb. Cortex *29*, 3224–3242.

Araya, R., Andino-Pavlovsky, V., Yuste, R., and Etchenique, R. (2013). Two-photon optical interrogation of individual dendritic spines with caged dopamine. ACS Chem. Neurosci. *4*, 1163–1167.

Arnsten, A.F.T., Wang, M.J., and Paspalas, C.D. (2012). Neuromodulation of thought: flexibilities and vulnerabilities in prefrontal cortical network synapses. Neuron *76*, 223–239.

Azdad, K., Gall, D., Woods, A.S., Ledent, C., Ferré, S., and Schiffmann, S.N. (2009). Dopamine D2 and adenosine A2A receptors regulate NMDA-mediated excitation in accumbens neurons through A2A-D2 receptor heteromerization. Neuropsychopharmacology *34*, 972–986.

Banasr, M., and Duman, R.S. (2008). Glial loss in the prefrontal cortex is sufficient to induce depressive-like behaviors. Biol. Psychiatry *64*, 863–870.

Banerjee, A., Lee, J., Nemcova, P., Liu, C., and Kaeser, P.S. (2020). Synaptotagmin-1 is the Ca2+ sensor for fast striatal dopamine release. Elife *9*.

Barbosa, J., Stein, H., Martinez, R.L., Galan-Gadea, A., Li, S., Dalmau, J., Adam, K.C.S., Valls-Solé, J., Constantinidis, C., and Compte, A. (2020). Interplay between persistent activity and activity-silent dynamics in the prefrontal cortex underlies serial biases in working memory. Nat. Neurosci. *23*, 1016–1024.

Batiuk, M.Y., Martirosyan, A., Wahis, J., de Vin, F., Marneffe, C., Kusserow, C., Koeppen, J., Viana,

J.F., Oliveira, J.F., Voet, T., et al. (2020). Identification of region-specific astrocyte subtypes at single cell resolution. Nat. Commun. *11*, 1220.

Bekar, L.K., He, W., and Nedergaard, M. (2008). Locus coeruleus alpha-adrenergic-mediated activation of cortical astrocytes in vivo. Cereb. Cortex *18*, 2789–2795.

Bender, C.L., Sun, X., Farooq, M., Yang, Q., Davison, C., Maroteaux, M., Huang, Y.-S., Ishikawa, Y., and Liu, S.J. (2020). Emotional Stress Induces Structural Plasticity in Bergmann Glial Cells via an AC5-CPEB3-GluA1 Pathway. J. Neurosci. *40*, 3374–3384.

Berger, B., Tassin, J.P., Blanc, G., Moyne, M.A., and Thierry, A.M. (1974). Histochemical confirmation for dopaminergic innervation of the rat cerebral cortex after destruction of the noradrenergic ascending pathways. Brain Res. *81*, 332–337.

Berridge, C.W., Devilbiss, D.M., Andrzejewski, M.E., Arnsten, A.F.T., Kelley, A.E., Schmeichel, B., Hamilton, C., and Spencer, R.C. (2006). Methylphenidate preferentially increases catecholamine neurotransmission within the prefrontal cortex at low doses that enhance cognitive function. Biol. Psychiatry *60*, 1111–1120.

Bezzi, P., Gundersen, V., Galbete, J.L., Seifert, G., Steinhäuser, C., Pilati, E., and Volterra, A. (2004). Astrocytes contain a vesicular compartment that is competent for regulated exocytosis of glutamate. Nat. Neurosci. *7*, 613–620.

Bonaventura, J., Rico, A.J., Moreno, E., Sierra, S., Sánchez, M., Luquin, N., Farré, D., Müller, C.E., Martínez-Pinilla, E., Cortés, A., et al. (2014). L-DOPA-treatment in primates disrupts the expression of A(2A) adenosine-CB(1) cannabinoid-D(2) dopamine receptor heteromers in the caudate nucleus. Neuropharmacology *79*, 90–100.

Brozoski, T.J., Brown, R.M., Rosvold, H.E., and Goldman, P.S. (1979). Cognitive deficit caused by regional depletion of dopamine in prefrontal cortex of rhesus monkey. Science *205*, 929–932.

Bushong, E.A., Martone, M.E., Jones, Y.Z., and Ellisman, M.H. (2002). Protoplasmic astrocytes in CA1 stratum radiatum occupy separate anatomical domains. J. Neurosci. *22*, 183–192.

Calebiro, D., Nikolaev, V.O., Gagliani, M.C., de Filippis, T., Dees, C., Tacchetti, C., Persani, L., and Lohse, M.J. (2009). Persistent cAMP-signals triggered by internalized G-protein-coupled receptors. PLoS Biol. *7*, e1000172.

Cao, X., Li, L.-P., Wang, Q., Wu, Q., Hu, H.-H., Zhang, M., Fang, Y.-Y., Zhang, J., Li, S.-J., Xiong, W.-C., et al. (2013). Astrocyte-derived ATP modulates depressive-like behaviors. Nat. Med. *19*, 773–777.

Cavanagh, S.E., Towers, J.P., Wallis, J.D., Hunt, L.T., and Kennerley, S.W. (2018). Reconciling persistent and dynamic hypotheses of working memory coding in prefrontal cortex. Nat. Commun. *9*, 3498.

Chai, H., Diaz-Castro, B., Shigetomi, E., Monte, E., Octeau, J.C., Yu, X., Cohn, W., Rajendran, P.S., Vondriska, T.M., Whitelegge, J.P., et al. (2017). Neural Circuit-Specialized Astrocytes: Transcriptomic, Proteomic, Morphological, and Functional Evidence. Neuron *95*, 531–549.e9.

Chen, L., Bohanick, J.D., Nishihara, M., Seamans, J.K., and Yang, C.R. (2007). Dopamine D1/5 receptor-mediated long-term potentiation of intrinsic excitability in rat prefrontal cortical neurons: Ca2+-dependent intracellular signaling. J. Neurophysiol. *97*, 2448–2464.

Cilz, N.I., Kurada, L., Hu, B., and Lei, S. (2014). Dopaminergic modulation of GABAergic transmission in the entorhinal cortex: concerted roles of α1 adrenoreceptors, inward rectifier K^+, and T-type Ca^{2+} channels. Cereb. Cortex *24*, 3195–3208.

Constantinidis, C., Funahashi, S., Lee, D., Murray, J.D., Qi, X.-L., Wang, M., and Arnsten, A.F.T. (2018). Persistent spiking activity underlies working memory. J. Neurosci. *38*, 7020–7028.

Corkrum, M., Covelo, A., Lines, J., Bellocchio, L., Pisansky, M., Loke, K., Quintana, R., Rothwell, P.E., Lujan, R., Marsicano, G., et al. (2020). Dopamine-Evoked Synaptic Regulation in the Nucleus Accumbens Requires Astrocyte Activity. Neuron *105*, 1036–1047.e5.

Cornil, C.A., and Ball, G.F. (2008). Interplay among catecholamine systems: dopamine binds to alpha2-adrenergic receptors in birds and mammals. J. Comp. Neurol. *511*, 610–627.

Cornil, C.A., Balthazart, J., Motte, P., Massotte, L., and Seutin, V. (2002). Dopamine activates noradrenergic receptors in the preoptic area. J. Neurosci. *22*, 9320–9330.

Courtney, N.A., and Ford, C.P. (2014). The timing of dopamine- and noradrenaline-mediated transmission reflects underlying differences in the extent of spillover and pooling. J. Neurosci. *34*, 7645–7656.

Cui, M., Aras, R., Christian, W.V., Rappold, P.M., Hatwar, M., Panza, J., Jackson-Lewis, V., Javitch, J.A., Ballatori, N., Przedborski, S., et al. (2009). The organic cation transporter-3 is a pivotal modulator of neurodegeneration in the nigrostriatal dopaminergic pathway. Proc. Natl. Acad. Sci. USA *106*, 8043–8048.

Cui, Q., Pitt, J.E., Pamukcu, A., Poulin, J.-F., Mabrouk, O.S., Fiske, M.P., Fan, I.B., Augustine, E.C., Young, K.A., Kennedy, R.T., et al. (2016). Blunted mGluR Activation Disinhibits Striatopallidal Transmission in Parkinsonian Mice. Cell Rep. *17*, 2431–2444.

D'Ascenzo, M., Fellin, T., Terunuma, M., Revilla-Sanchez, R., Meaney, D.F., Auberson, Y.P., Moss, S.J., and Haydon, P.G. (2007). mGluR5 stimulates gliotransmission in the nucleus accumbens. Proc. Natl. Acad. Sci. USA *104*, 1995–2000.

Devoto, P., Flore, G., Saba, P., Fà, M., and Gessa, G.L. (2005). Co-release of noradrenaline and dopamine in the cerebral cortex elicited by single train and repeated train stimulation of the locus coeruleus. BMC Neurosci. *6*, 31.

Dias, R., Robbins, T.W., and Roberts, A.C. (1996). Primate analogue of the Wisconsin Card Sorting Test: effects of excitotoxic lesions of the prefrontal cortex in the marmoset. Behav. Neurosci. *110*, 872–886.

Ding, F., O'Donnell, J., Thrane, A.S., Zeppenfeld, D., Kang, H., Xie, L., Wang, F., and Nedergaard, M. (2013). α1-Adrenergic receptors mediate coordinated Ca2+ signaling of cortical astrocytes in awake, behaving mice. Cell Calcium *54*, 387–394.

Dos Santos Pereira, J.N., Tadjerpisheh, S., Abu Abed, M., Saadatmand, A.R., Weksler, B., Romero, I.A., Couraud, P.-O., Brockmöller, J., and Tzvetkov, M.V. (2014). The poorly membrane permeable antipsychotic drugs amisulpride and sulpiride are substrates of the organic cation transporters from the SLC22 family. AAPS J. *16*, 1247–1258.

Duan, H., and Wang, J. (2010). Selective transport of monoamine neurotransmitters by human plasma membrane monoamine transporter and organic cation transporter 3. J. Pharmacol. Exp. Ther. *335*, 743–753.

Dubbs, A., Guevara, J., and Yuste, R. (2016). moco: Fast Motion Correction for Calcium Imaging. Front Neuroinformatics *10*, 6.

Edelmann, E., and Lessmann, V. (2018). Dopaminergic innervation and modulation of hippocampal networks. Cell Tissue Res. *373*, 711–727.

Feng, J., Zhang, C., Lischinsky, J.E., Jing, M., Zhou, J., Wang, H., Zhang, Y., Dong, A., Wu, Z., Wu, H., et al. (2019). A genetically encoded fluorescent sensor for rapid and specific in vivo detection of norepinephrine. Neuron *102*, 745–761.e8.

Fischer, T., Scheffler, P., and Lohr, C. (2020). Dopamine-induced calcium signaling in olfactory bulb astrocytes. Sci. Rep. *10*, 631.

Frederick, A.L., Yano, H., Trifilieff, P., Vishwasrao, H.D., Biezonski, D., Mészáros, J., Urizar, E., Sibley, D.R., Kellendonk, C., Sonntag, K.C., et al. (2015). Evidence against dopamine D1/D2 receptor heteromers. Mol. Psychiatry *20*, 1373–1385.

Fritschy, J.M., and Grzanna, R. (1989). Immunohistochemical analysis of the neurotoxic effects of DSP-4 identifies two populations of noradrenergic axon terminals. Neuroscience *30*, 181–197.

Funahashi, S., Bruce, C.J., and Goldman-Rakic, P.S. (1989). Mnemonic coding of visual space in the monkey's dorsolateral prefrontal cortex. J. Neurophysiol. *61*, 331–349.

Fuster, J.M., and Alexander, G.E. (1971). Neuron activity related to short-term memory. Science *173*, 652–654.

Fuster, J.M., Bodner, M., and Kroger, J.K. (2000). Cross-modal and cross-temporal association in neurons of frontal cortex. Nature *405*, 347–351.

Gao, W.-J., and Goldman-Rakic, P.S. (2003). Selective modulation of excitatory and inhibitory

microcircuits by dopamine. Proc. Natl. Acad. Sci. USA *100*, 2836–2841.

Gao, W.-J., Wang, Y., and Goldman-Rakic, P.S. (2003). Dopamine modulation of perisomatic and peridendritic inhibition in prefrontal cortex. J. Neurosci. *23*, 1622–1630.

Garris, P.A., and Wightman, R.M. (1994). Different kinetics govern dopaminergic transmission in the amygdala, prefrontal cortex, and striatum: an in vivo voltammetric study. J. Neurosci. *14*, 442–450.

George, M.S., Ketter, T.A., Parekh, P.I., Horwitz, B., Herscovitch, P., and Post, R.M. (1995). Brain activity during transient sadness and happiness in healthy women. Am. J. Psychiatry *152*, 341–351.

Goldman-Rakic, P.S. (1995). Cellular basis of working memory. Neuron *14*, 477–485.

Gong, S., Zheng, C., Doughty, M.L., Losos, K., Didkovsky, N., Schambra, U.B., Nowak, N.J., Joyner, A., Leblanc, G., Hatten, M.E., et al. (2003). A gene expression atlas of the central nervous system based on bacterial artificial chromosomes. Nature *425*, 917–925.

González, S., Moreno-Delgado, D., Moreno, E., Pérez-Capote, K., Franco, R., Mallol, J., Cortés, A., Casadó, V., Lluís, C., Ortiz, J., et al. (2012). Circadian-related heteromerization of adrenergic and dopamine D_4 receptors modulates melatonin synthesis and release in the pineal gland. PLoS Biol. *10*, e1001347.

Gordon, G.R.J., Baimoukhametova, D.V., Hewitt, S.A., Rajapaksha, W.R.A.K.J.S., Fisher, T.E., and Bains, J.S. (2005). Norepinephrine triggers release of glial ATP to increase postsynaptic efficacy. Nat. Neurosci. *8*, 1078–1086.

Gresch, P.J., Sved, A.F., Zigmond, M.J., and Finlay, J.M. (1994). Stress-induced sensitization of dopamine and norepinephrine efflux in medial prefrontal cortex of the rat. J. Neurochem. *63*, 575–583.

Guiard, B.P., El Mansari, M., and Blier, P. (2008). Cross-talk between dopaminergic and noradrenergic systems in the rat ventral tegmental area, locus ceruleus, and dorsal hippocampus. Mol. Pharmacol. *74*, 1463–1475.

Harada, K., Ito, M., Wang, X., Tanaka, M., Wongso, D., Konno, A., Hirai, H., Hirase, H., Tsuboi, T., and Kitaguchi, T. (2017). Red fluorescent protein-based cAMP indicator applicable to optogenetics and in vivo imaging. Sci. Rep. *7*, 7351.

Hariri, A.R., Mattay, V.S., Tessitore, A., Fera, F., and Weinberger, D.R. (2003). Neocortical modulation of the amygdala response to fearful stimuli. Biol. Psychiatry *53*, 494–501.

Huang, Y.-Y., Simpson, E., Kellendonk, C., and Kandel, E.R. (2004). Genetic evidence for the bidirectional modulation of synaptic plasticity in the prefrontal cortex by D1 receptors. Proc. Natl. Acad. Sci. USA *101*, 3236–3241.

Hurst, J.L., and West, R.S. (2010). Taming anxiety in laboratory mice. Nat. Methods *7*, 825–826.

Inagaki, H.K., Fontolan, L., Romani, S., and Svoboda, K. (2019). Discrete attractor dynamics underlies

persistent activity in the frontal cortex. Nature *566*, 212–217.

Irannejad, R., Tomshine, J.C., Tomshine, J.R., Chevalier, M., Mahoney, J.P., Steyaert, J., Rasmussen, S.G.F., Sunahara, R.K., El-Samad, H., Huang, B., et al. (2013). Conformational biosensors reveal GPCR signalling from endosomes. Nature *495*, 534–538.

Jennings, A., Tyurikova, O., Bard, L., Zheng, K., Semyanov, A., Henneberger, C., and Rusakov, D.A. (2017). Dopamine elevates and lowers astroglial Ca2+ through distinct pathways depending on local synaptic circuitry. Glia *65*, 447–459.

John, C.S., Smith, K.L., Van't Veer, A., Gompf, H.S., Carlezon, W.A., Cohen, B.M., Öngür, D., and Bechtholt-Gompf, A.J. (2012). Blockade of astrocytic glutamate uptake in the prefrontal cortex induces anhedonia. Neuropsychopharmacology *37*, 2467–2475.

Kamigaki, T., and Dan, Y. (2017). Delay activity of specific prefrontal interneuron subtypes modulates memory-guided behavior. Nat. Neurosci. *20*, 854–863.

Kempadoo, K.A., Mosharov, E.V., Choi, S.J., Sulzer, D., and Kandel, E.R. (2016). Dopamine release from the locus coeruleus to the dorsal hippocampus promotes spatial learning and memory. Proc. Natl. Acad. Sci. USA *113*, 14835–14840.

Kesner, R.P., Hunt, M.E., Williams, J.M., and Long, J.M. (1996). Prefrontal cortex and working memory for spatial response, spatial location, and visual object information in the rat. Cereb. Cortex *6*, 311–318.

Khakh, B.S., and Sofroniew, M.V. (2015). Diversity of astrocyte functions and phenotypes in neural circuits. Nat. Neurosci. *18*, 942–952.

Kim, D., Jeong, H., Lee, J., Ghim, J.-W., Her, E.S., Lee, S.-H., and Jung, M.W. (2016). Distinct Roles of Parvalbumin- and Somatostatin-Expressing Interneurons in Working Memory. Neuron *92*, 902–915.

Kim, H., Somerville, L.H., Johnstone, T., Alexander, A.L., and Whalen, P.J. (2003). Inverse amygdala and medial prefrontal cortex responses to surprised faces. Neuroreport *14*, 2317–2322.

Kirshner, N. (1957). Pathway of noradrenaline formation from DOPA. J. Biol. Chem. *226*, 821–825.

Kofuji, P., and Araque, A. (2021). G-Protein-Coupled Receptors in Astrocyte-Neuron Communication. Neuroscience *456*, 71–84.

Kol, A., Adamsky, A., Groysman, M., Kreisel, T., London, M., and Goshen, I. (2020). Astrocytes contribute to remote memory formation by modulating hippocampal-cortical communication during learning. Nat. Neurosci. *23*, 1229–1239.

Kolasa, M., Solich, J., Faron-Górecka, A., Żurawek, D., Pabian, P., Łukasiewicz, S., Kuśmider, M., Szafran-Pilch, K., Szlachta, M., and Dziedzicka-Wasylewska, M. (2018). Paroxetine and Low-dose Risperidone Induce Serotonin 5-HT1A and Dopamine D2 Receptor Heteromerization in the Mouse Prefrontal Cortex. Neuroscience *377*, 184–196.

Kotowski, S.J., Hopf, F.W., Seif, T., Bonci, A., and von Zastrow, M. (2011). Endocytosis promotes rapid dopaminergic signaling. Neuron *71*, 278–290.

Kröner, S., Krimer, L.S., Lewis, D.A., and Barrionuevo, G. (2007). Dopamine increases inhibition in the monkey dorsolateral prefrontal cortex through cell type-specific modulation of interneurons. Cereb. Cortex *17*, 1020–1032.

Lalo, U., Palygin, O., Rasooli-Nejad, S., Andrew, J., Haydon, P.G., and Pankratov, Y. (2014). Exocytosis of ATP from astrocytes modulates phasic and tonic inhibition in the neocortex. PLoS Biol. *12*, e1001747.

Lammel, S., Hetzel, A., Häckel, O., Jones, I., Liss, B., and Roeper, J. (2008). Unique properties of mesoprefrontal neurons within a dual mesocorticolimbic dopamine system. Neuron *57*, 760–773.

Lammel, S., Lim, B.K., Ran, C., Huang, K.W., Betley, M.J., Tye, K.M., Deisseroth, K., and Malenka, R.C. (2012). Input-specific control of reward and aversion in the ventral tegmental area. Nature *491*, 212–217.

Lanjakornsiripan, D., Pior, B.-J., Kawaguchi, D., Furutachi, S., Tahara, T., Katsuyama, Y., Suzuki, Y., Fukazawa, Y., and Gotoh, Y. (2018). Layer-specific morphological and molecular differences in neocortical astrocytes and their dependence on neuronal layers. Nat. Commun. *9*, 1623.

Lee, S.J., Lodder, B., Chen, Y., Patriarchi, T., Tian, L., and Sabatini, B.L. (2021). Cell-type-specific asynchronous modulation of PKA by dopamine in learning. Nature *590*, 451–456.

Lee, S.P., So, C.H., Rashid, A.J., Varghese, G., Cheng, R., Lança, A.J., O'Dowd, B.F., and George, S.R. (2004). Dopamine D1 and D2 receptor Co-activation generates a novel phospholipase C-mediated calcium signal. J. Biol. Chem. *279*, 35671–35678.

Lee, Y., Son, H., Kim, G., Kim, S., Lee, D.H., Roh, G.S., Kang, S.S., Cho, G.J., Choi, W.S., and Kim, H.J. (2013). Glutamine deficiency in the prefrontal cortex increases depressive-like behaviours in male mice. J. Psychiatry Neurosci. *38*, 183–191.

Levene, M.J., Dombeck, D.A., Kasischke, K.A., Molloy, R.P., and Webb, W.W. (2004). In vivo multiphoton microscopy of deep brain tissue. J. Neurophysiol. *91*, 1908–1912.

Li, X., Zima, A.V., Sheikh, F., Blatter, L.A., and Chen, J. (2005). Endothelin-1-induced arrhythmogenic Ca2+ signaling is abolished in atrial myocytes of inositol-1,4,5-trisphosphate(IP3)-receptor type 2-deficient mice. Circ. Res. *96*, 1274–1281.

Lima, A., Sardinha, V.M., Oliveira, A.F., Reis, M., Mota, C., Silva, M.A., Marques, F., Cerqueira, J.J., Pinto, L., Sousa, N., et al. (2014). Astrocyte pathology in the prefrontal cortex impairs the cognitive function of rats. Mol. Psychiatry *19*, 834–841.

Lohani, S., Martig, A.K., Deisseroth, K., Witten, I.B., and Moghaddam, B. (2019). Dopamine modulation of prefrontal cortex activity is manifold and operates at multiple temporal and spatial scales. Cell Rep.

27, 99–114.e6.

Marek, G.J., and Aghajanian, G.K. (1999). 5-HT2A receptor or alpha1-adrenoceptor activation induces excitatory postsynaptic currents in layer V pyramidal cells of the medial prefrontal cortex. Eur. J. Pharmacol. *367*, 197–206.

Martín, R., Bajo-Grañeras, R., Moratalla, R., Perea, G., and Araque, A. (2015). Circuit-specific signaling in astrocyte-neuron networks in basal ganglia pathways. Science *349*, 730–734.

Martin-Fernandez, M., Jamison, S., Robin, L.M., Zhao, Z., Martin, E.D., Aguilar, J., Benneyworth, M.A., Marsicano, G., and Araque, A. (2017). Synapse-specific astrocyte gating of amygdala-related behavior. Nat. Neurosci. *20*, 1540–1548.

Matsuda, Y., Marzo, A., and Otani, S. (2006). The presence of background dopamine signal converts long-term synaptic depression to potentiation in rat prefrontal cortex. J. Neurosci. *26*, 4803–4810.

Mederos, S., Sánchez-Puelles, C., Esparza, J., Valero, M., Ponomarenko, A., and Perea, G. (2021). GABAergic signaling to astrocytes in the prefrontal cortex sustains goal-directed behaviors. Nat. Neurosci. *24*, 82–92.

Medvedev, I.O., Ramsey, A.J., Masoud, S.T., Bermejo, M.K., Urs, N., Sotnikova, T.D., Beaulieu, J.-M., Gainetdinov, R.R., and Salahpour, A. (2013). D1 dopamine receptor coupling to PLCβ regulates forward locomotion in mice. J. Neurosci. *33*, 18125–18133.

Milad, M.R., and Quirk, G.J. (2002). Neurons in medial prefrontal cortex signal memory for fear extinction. Nature *420*, 70–74.

Mitrano, D.A., Pare, J.F., Smith, Y., and Weinshenker, D. (2014). D1-dopamine and α1-adrenergic receptors co-localize in dendrites of the rat prefrontal cortex. Neuroscience *258*, 90–100.

Moreno, E., Moreno-Delgado, D., Navarro, G., Hoffmann, H.M., Fuentes, S., Rosell-Vilar, S., Gasperini, P., Rodríguez-Ruiz, M., Medrano, M., Mallol, J., et al. (2014). Cocaine disrupts histamine H3 receptor modulation of dopamine D1 receptor signaling: σ1-D1-H3 receptor complexes as key targets for reducing cocaine's effects. J. Neurosci. *34*, 3545–3558.

Morón, J.A., Brockington, A., Wise, R.A., Rocha, B.A., and Hope, B.T. (2002). Dopamine uptake through the norepinephrine transporter in brain regions with low levels of the dopamine transporter: evidence from knock-out mouse lines. J. Neurosci. *22*, 389–395.

Muller, A., Joseph, V., Slesinger, P.A., and Kleinfeld, D. (2014). Cell-based reporters reveal in vivo dynamics of dopamine and norepinephrine release in murine cortex. Nat. Methods *11*, 1245–1252.

Muntean, B.S., Zucca, S., MacMullen, C.M., Dao, M.T., Johnston, C., Iwamoto, H., Blakely, R.D., Davis, R.L., and Martemyanov, K.A. (2018). Interrogating the Spatiotemporal Landscape of Neuromodulatory GPCR Signaling by Real-Time Imaging of cAMP in Intact Neurons and Circuits. Cell Rep. *22*, 255–268.

Murphy-Royal, C., Johnston, A.D., Boyce, A.K.J., Diaz-Castro, B., Institoris, A., Peringod, G., Zhang, O., Stout, R.F., Spray, D.C., Thompson, R.J., et al. (2020). Stress gates an astrocytic energy reservoir to impair synaptic plasticity. Nat. Commun. *11*, 2014.

Nagai, J., Rajbhandari, A.K., Gangwani, M.R., Hachisuka, A., Coppola, G., Masmanidis, S.C., Fanselow, M.S., and Khakh, B.S. (2019). Hyperactivity with Disrupted Attention by Activation of an Astrocyte Synaptogenic Cue. Cell *177*, 1280–1292.e20.

Navarro, G., Cordomí, A., Casadó-Anguera, V., Moreno, E., Cai, N.-S., Cortés, A., Canela, E.I., Dessauer, C.W., Casadó, V., Pardo, L., et al. (2018). Evidence for functional pre-coupled complexes of receptor heteromers and adenylyl cyclase. Nat. Commun. *9*, 1242.

Nicola, S.M., and Malenka, R.C. (1997). Dopamine depresses excitatory and inhibitory synaptic transmission by distinct mechanisms in the nucleus accumbens. J. Neurosci. *17*, 5697–5710.

Nomura, S., Bouhadana, M., Morel, C., Faure, P., Cauli, B., Lambolez, B., and Hepp, R. (2014). Noradrenalin and dopamine receptors both control cAMP-PKA signaling throughout the cerebral cortex. Front. Cell Neurosci. *8*, 247.

Oe, Y., Wang, X., Patriarchi, T., Konno, A., Ozawa, K., Yahagi, K., Hirai, H., Tsuboi, T., Kitaguchi, T., Tian, L., et al. (2020). Distinct temporal integration of noradrenaline signaling by astrocytic second messengers during vigilance. Nat. Commun. *11*, 471.

Özkan, M., Johnson, N.W., Sehirli, U.S., Woodhall, G.L., and Stanford, I.M. (2017). Dopamine acting at D1-like, D2-like and α1-adrenergic receptors differentially modulates theta and gamma oscillatory activity in primary motor cortex. PLoS One *12*, e0181633.

Panatier, A., Vallée, J., Haber, M., Murai, K.K., Lacaille, J.-C., and Robitaille, R. (2011). Astrocytes are endogenous regulators of basal transmission at central synapses. Cell *146*, 785–798.

Pankratov, Y., and Lalo, U. (2015). Role for astroglial α1-adrenoreceptors in gliotransmission and control of synaptic plasticity in the neocortex. Front. Cell Neurosci. *9*, 230.

Park, J.C., Bae, J.W., Kim, J., and Jung, M.W. (2019). Dynamically changing neuronal activity supporting working memory for predictable and unpredictable durations. Sci. Rep. *9*, 15512.

Pascual, O., Casper, K.B., Kubera, C., Zhang, J., Revilla-Sanchez, R., Sul, J.-Y., Takano, H., Moss, S.J., McCarthy, K., and Haydon, P.G. (2005). Astrocytic purinergic signaling coordinates synaptic networks. Science *310*, 113–116.

Patriarchi, T., Cho, J.R., Merten, K., Howe, M.W., Marley, A., Xiong, W.-H., Folk, R.W., Broussard, G.J., Liang, R., Jang, M.J., et al. (2018). Ultrafast neuronal imaging of dopamine dynamics with designed genetically encoded sensors. Science *360*.

Patriarchi, T., Mohebi, A., Sun, J., Marley, A., Liang, R., Dong, C., Puhger, K., Mizuno, G.O., Davis, C.M., Wiltgen, B., et al. (2020). An expanded palette of dopamine sensors for multiplex imaging in

vivo. Nat. Methods *17*, 1147–1155.

Paukert, M., Agarwal, A., Cha, J., Doze, V.A., Kang, J.U., and Bergles, D.E. (2014). Norepinephrine controls astroglial responsiveness to local circuit activity. Neuron *82*, 1263–1270.

Pelassa, S., Guidolin, D., Venturini, A., Averna, M., Frumento, G., Campanini, L., Bernardi, R., Cortelli, P., Buonaura, G.C., Maura, G., et al. (2019). A2A-D2 Heteromers on Striatal Astrocytes: Biochemical and Biophysical Evidence. Int. J. Mol. Sci. *20*.

Perea, G., and Araque, A. (2007). Astrocytes potentiate transmitter release at single hippocampal synapses. Science *317*, 1083–1086.

Petravicz, J., Fiacco, T.A., and McCarthy, K.D. (2008). Loss of IP3 receptor-dependent Ca2+ increases in hippocampal astrocytes does not affect baseline CA1 pyramidal neuron synaptic activity. J. Neurosci. *28*, 4967–4973.

Petrelli, F., Dallérac, G., Pucci, L., Calì, C., Zehnder, T., Sultan, S., Lecca, S., Chicca, A., Ivanov, A., Asensio, C.S., et al. (2020). Dysfunction of homeostatic control of dopamine by astrocytes in the developing prefrontal cortex leads to cognitive impairments. Mol. Psychiatry *25*, 732–749.

Pinto, L., and Dan, Y. (2015). Cell-Type-Specific Activity in Prefrontal Cortex during Goal-Directed Behavior. Neuron *87*, 437–450.

Porter, J.T., and McCarthy, K.D. (1997). Astrocytic neurotransmitter receptors in situ and in vivo. Prog. Neurobiol. *51*, 439–455.

Poskanzer, K.E., and Yuste, R. (2016). Astrocytes regulate cortical state switching in vivo. Proc. Natl. Acad. Sci. USA *113*, E2675-84.

Pougnet, J.-T., Toulme, E., Martinez, A., Choquet, D., Hosy, E., and Boué-Grabot, E. (2014). ATP P2X receptors downregulate AMPA receptor trafficking and postsynaptic efficacy in hippocampal neurons. Neuron *83*, 417–430.

Proudman, R.G.W., and Baker, J.G. (2021). The selectivity of α-adrenoceptor agonists for the human α1A, α1B, and α1D-adrenoceptors. Pharmacol. Res. Perspect. *9*, e00799.

Ragozzino, M.E., Detrick, S., and Kesner, R.P. (1999). Involvement of the prelimbic-infralimbic areas of the rodent prefrontal cortex in behavioral flexibility for place and response learning. J. Neurosci. *19*, 4585–4594.

Rebois, R.V., Maki, K., Meeks, J.A., Fishman, P.H., Hébert, T.E., and Northup, J.K. (2012). D2-like dopamine and β-adrenergic receptors form a signaling complex that integrates Gs- and Gi-mediated regulation of adenylyl cyclase. Cell Signal. *24*, 2051–2060.

Rosenkranz, J.A., and Grace, A.A. (2001). Dopamine attenuates prefrontal cortical suppression of sensory inputs to the basolateral amygdala of rats. J. Neurosci. *21*, 4090–4103.

Sahu, A., Tyeryar, K.R., Vongtau, H.O., Sibley, D.R., and Undieh, A.S. (2009). D5 dopamine receptors

are required for dopaminergic activation of phospholipase C. Mol. Pharmacol. *75*, 447–453.

Sardinha, V.M., Guerra-Gomes, S., Caetano, I., Tavares, G., Martins, M., Reis, J.S., Correia, J.S., Teixeira-Castro, A., Pinto, L., Sousa, N., et al. (2017). Astrocytic signaling supports hippocampal-prefrontal theta synchronization and cognitive function. Glia *65*, 1944–1960.

Seamans, J.K., Gorelova, N., Durstewitz, D., and Yang, C.R. (2001). Bidirectional dopamine modulation of GABAergic inhibition in prefrontal cortical pyramidal neurons. J. Neurosci. *21*, 3628–3638.

Sesack, S.R., Hawrylak, V.A., Matus, C., Guido, M.A., and Levey, A.I. (1998). Dopamine axon varicosities in the prelimbic division of the rat prefrontal cortex exhibit sparse immunoreactivity for the dopamine transporter. J. Neurosci. *18*, 2697–2708.

Shigetomi, E., Kracun, S., Sofroniew, M.V., and Khakh, B.S. (2010). A genetically targeted optical sensor to monitor calcium signals in astrocyte processes. Nat. Neurosci. *13*, 759–766.

Shuen, J.A., Chen, M., Gloss, B., and Calakos, N. (2008). Drd1a-tdTomato BAC transgenic mice for simultaneous visualization of medium spiny neurons in the direct and indirect pathways of the basal ganglia. J. Neurosci. *28*, 2681–2685.

Simard, S., Coppola, G., Rudyk, C.A., Hayley, S., McQuaid, R.J., and Salmaso, N. (2018). Profiling changes in cortical astroglial cells following chronic stress. Neuropsychopharmacology *43*, 1961–1971.

Slezak, M., Kandler, S., Van Veldhoven, P.P., Van den Haute, C., Bonin, V., and Holt, M.G. (2019). Distinct Mechanisms for Visual and Motor-Related Astrocyte Responses in Mouse Visual Cortex. Curr. Biol. *29*, 3120–3127.e5.

Smith, C.C., and Greene, R.W. (2012). CNS dopamine transmission mediated by noradrenergic innervation. J. Neurosci. *32*, 6072–6080.

Spaak, E., Watanabe, K., Funahashi, S., and Stokes, M.G. (2017). Stable and dynamic coding for working memory in primate prefrontal cortex. J. Neurosci. *37*, 6503–6516.

Srinivasan, R., Lu, T.-Y., Chai, H., Xu, J., Huang, B.S., Golshani, P., Coppola, G., and Khakh, B.S. (2016). New transgenic mouse lines for selectively targeting astrocytes and studying calcium signals in astrocyte processes in situ and in vivo. Neuron *92*, 1181–1195.

Stanford, S.C., and Heal, D.J. (2019). Catecholamines: Knowledge and understanding in the 1960s, now, and in the future. Brain Neurosci. Adv. *3*, 2398212818810682.

Steinberg, S.F., and Bilezikian, J.P. (1982). Identification and characterization of alpha 1 adrenergic receptors in rat myocardium with a new iodinated radioligand, [125I]IBE 2254. J. Mol. Cell Cardiol. *14*, 601–610.

Sun, F., Zeng, J., Jing, M., Zhou, J., Feng, J., Owen, S.F., Luo, Y., Li, F., Wang, H., Yamaguchi, T., et al. (2018). A genetically encoded fluorescent sensor enables rapid and specific detection of dopamine in

flies, fish, and mice. Cell *174*, 481–496.e19.

Takeuchi, T., Duszkiewicz, A.J., Sonneborn, A., Spooner, P.A., Yamasaki, M., Watanabe, M., Smith, C.C., Fernández, G., Deisseroth, K., Greene, R.W., et al. (2016). Locus coeruleus and dopaminergic consolidation of everyday memory. Nature *537*, 357–362.

Thierry, A.M., Tassin, J.P., Blanc, G., and Glowinski, J. (1976). Selective activation of mesocortical DA system by stress. Nature *263*, 242–244.

Trifilieff, P., Rives, M.-L., Urizar, E., Piskorowski, R.A., Vishwasrao, H.D., Castrillon, J., Schmauss, C., Slättman, M., Gullberg, M., and Javitch, J.A. (2011). Detection of antigen interactions ex vivo by proximity ligation assay: endogenous dopamine D2-adenosine A2A receptor complexes in the striatum. BioTechniques *51*, 111–118.

Tsai, H.-H., Li, H., Fuentealba, L.C., Molofsky, A.V., Taveira-Marques, R., Zhuang, H., Tenney, A., Murnen, A.T., Fancy, S.P.J., Merkle, F., et al. (2012). Regional astrocyte allocation regulates CNS synaptogenesis and repair. Science *337*, 358–362.

Undie, A.S., and Friedman, E. (1990). Stimulation of a dopamine D1 receptor enhances inositol phosphates formation in rat brain. J. Pharmacol. Exp. Ther. *253*, 987–992.

Valle-León, M., Callado, L.F., Aso, E., Cajiao-Manrique, M.M., Sahlholm, K., López-Cano, M., Soler, C., Altafaj, X., Watanabe, M., Ferré, S., et al. (2021). Decreased striatal adenosine A2A-dopamine D2 receptor heteromerization in schizophrenia. Neuropsychopharmacology *46*, 665–672.

Vander Weele, C.M., Siciliano, C.A., Matthews, G.A., Namburi, P., Izadmehr, E.M., Espinel, I.C., Nieh, E.H., Schut, E.H.S., Padilla-Coreano, N., Burgos-Robles, A., et al. (2018). Dopamine enhances signal-to-noise ratio in cortical-brainstem encoding of aversive stimuli. Nature *563*, 397–401.

Vijayraghavan, S., Wang, M., Birnbaum, S.G., Williams, G.V., and Arnsten, A.F.T. (2007). Inverted-U dopamine D1 receptor actions on prefrontal neurons engaged in working memory. Nat. Neurosci. *10*, 376–384.

Wang, Q., Kong, Y., Wu, D.-Y., Liu, J.-H., Jie, W., You, Q.-L., Huang, L., Hu, J., Chu, H.-D., Gao, F., et al. (2021). Impaired calcium signaling in astrocytes modulates autism spectrum disorder-like behaviors in mice. Nat. Commun. *12*, 3321.

Wang, Y., DelRosso, N.V., Vaidyanathan, T.V., Cahill, M.K., Reitman, M.E., Pittolo, S., Mi, X., Yu, G., and Poskanzer, K.E. (2019). Accurate quantification of astrocyte and neurotransmitter fluorescence dynamics for single-cell and population-level physiology. Nat. Neurosci. *22*, 1936–1944.

Wu, Z., He, K., Chen, Y., Li, H., Pan, S., Li, B., Liu, T., Wang, H., Du, J., Jing, M., et al. (2021). An ultrasensitive GRAB sensor for detecting extracellular ATP in vitro and in vivo. BioRxiv.

Xin, W., Schuebel, K.E., Jair, K.-W., Cimbro, R., De Biase, L.M., Goldman, D., and Bonci, A. (2019). Ventral midbrain astrocytes display unique physiological features and sensitivity to dopamine D2

receptor signaling. Neuropsychopharmacology *44*, 344–355.

Yang, J., Vitery, M.D.C., Chen, J., Osei-Owusu, J., Chu, J., and Qiu, Z. (2019). Glutamate-Releasing SWELL1 Channel in Astrocytes Modulates Synaptic Transmission and Promotes Brain Damage in Stroke. Neuron *102*, 813–827.e6.

Yapo, C., Nair, A.G., Clement, L., Castro, L.R., Hellgren Kotaleski, J., and Vincent, P. (2017). Detection of phasic dopamine by D1 and D2 striatal medium spiny neurons. J. Physiol. (Lond.) *595*, 7451–7475.

Zhang, J., Wang, H., Ye, C., Ge, W., Chen, Y., Jiang, Z., Wu, C., Poo, M., and Duan, S. (2003). ATP released by astrocytes mediates glutamatergic activity-dependent heterosynaptic suppression. Neuron *40*, 971–982.

Zhang, Y., Chen, K., Sloan, S.A., Bennett, M.L., Scholze, A.R., O'Keeffe, S., Phatnani, H.P., Guarnieri, P., Caneda, C., Ruderisch, N., et al. (2014). An RNA-sequencing transcriptome and splicing database of glia, neurons, and vascular cells of the cerebral cortex. J. Neurosci. *34*, 11929–11947.

Zhu, Y., Dwork, A.J., Trifilieff, P., and Javitch, J.A. (2020). Detection of G Protein-Coupled Receptor Complexes in Postmortem Human Brain by Proximity Ligation Assay. Curr Protoc Neurosci *91*, e86.

Zwart, R., Verhaagh, S., Buitelaar, M., Popp-Snijders, C., and Barlow, D.P. (2001). Impaired activity of the extraneuronal monoamine transporter system known as uptake-2 in Orct3/Slc22a3-deficient mice. Mol. Cell. Biol. *21*, 4188–4196.

Supplemental Information

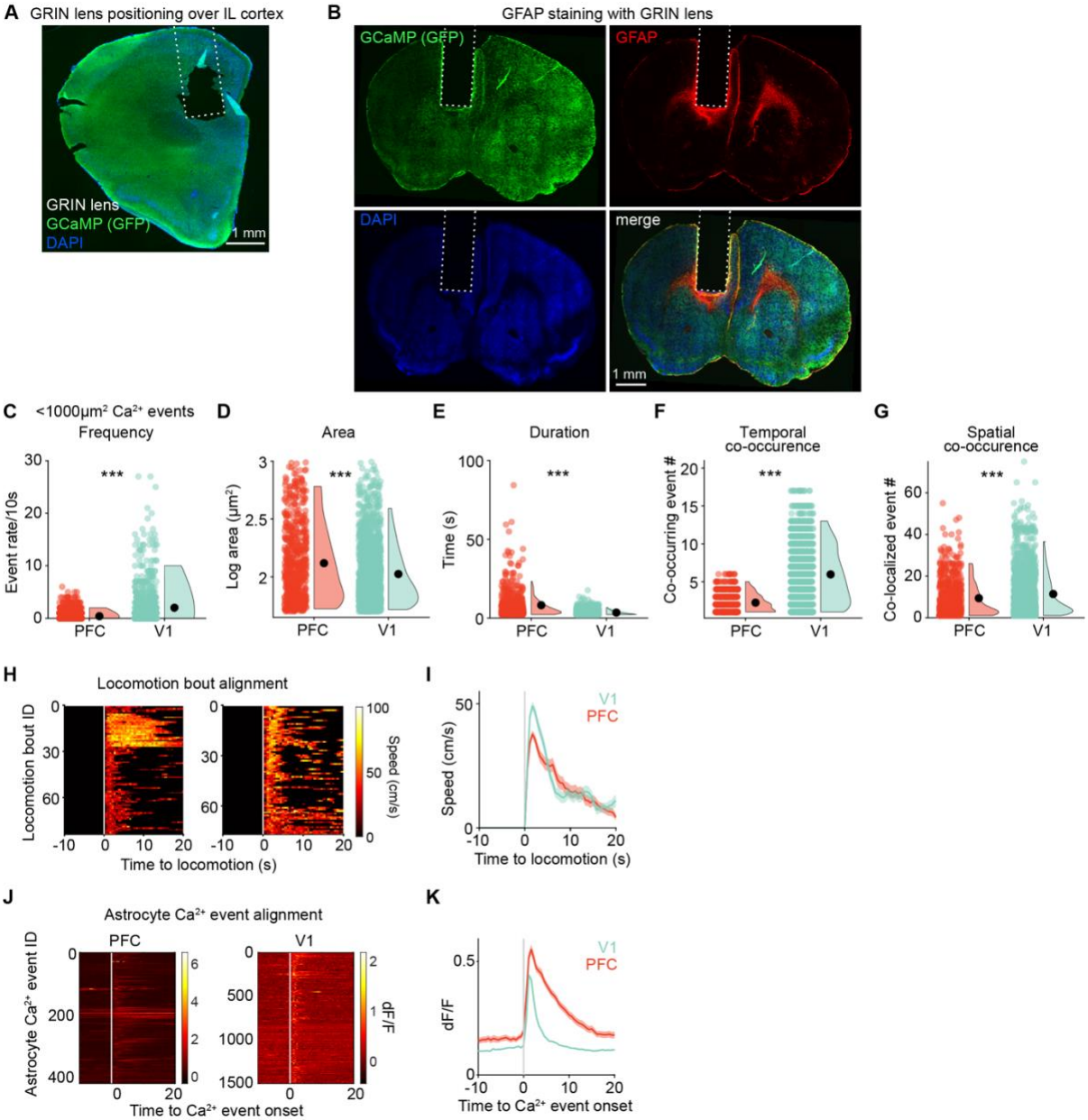

Figure S1, Further comparison of *in vivo* astrocyte Ca^{2+} in V1 and PFC, Related to Fig. 1. (A) GRIN lens implant location in PFC was confirmed by fixation and sectioning (~2 mm anterior from Bregma), immunostaining to visualize astrocytic expression of Lck-GCaMP (green) and DAPI (blue) for nuclei. **(B)** GFAP (red), astrocytic Lck-GCaMP (green), and nuclei staining (DAPI, blue) were used to assess astrocyte reactivity around implanted GRIN lenses. **(C–G)** Small (<1000μm^2) astrocyte Ca^{2+}-event features also vary between brain regions. Small events occur at lower rates in PFC (C), but are (D) larger and (E) longer than those in V1. Small events in PFC (F) co-occur with other events less than in V1, but (G) tend to repeat less at the same spatial location. Data shown as all bins/events (colored dots), 5th–95th percentile distribution (violins), and mean±sem (black dots and error bars). Wilcoxon rank-sum test; ***, $p<10^{-5}$. PFC: n=1486 60-s bins, 593 events, 4 mice; V1: n=780 60-s bins, 1561 events, 3 mice. **(H–I)** Animal speed (cm/s) aligned to start of locomotion bouts (t=0), shown as heat map for all locomotion bouts (H) and average traces±sem (I), for data shown in Fig. 1 J–K. **(J–K)** Astrocyte Ca^{2+} traces (dF/F) aligned to the onset of the AQuA-detected Ca^{2+} events (t=0), shown as heatmaps for all events (J) and average traces±sem (K), for data shown in Fig. 1 L–M.

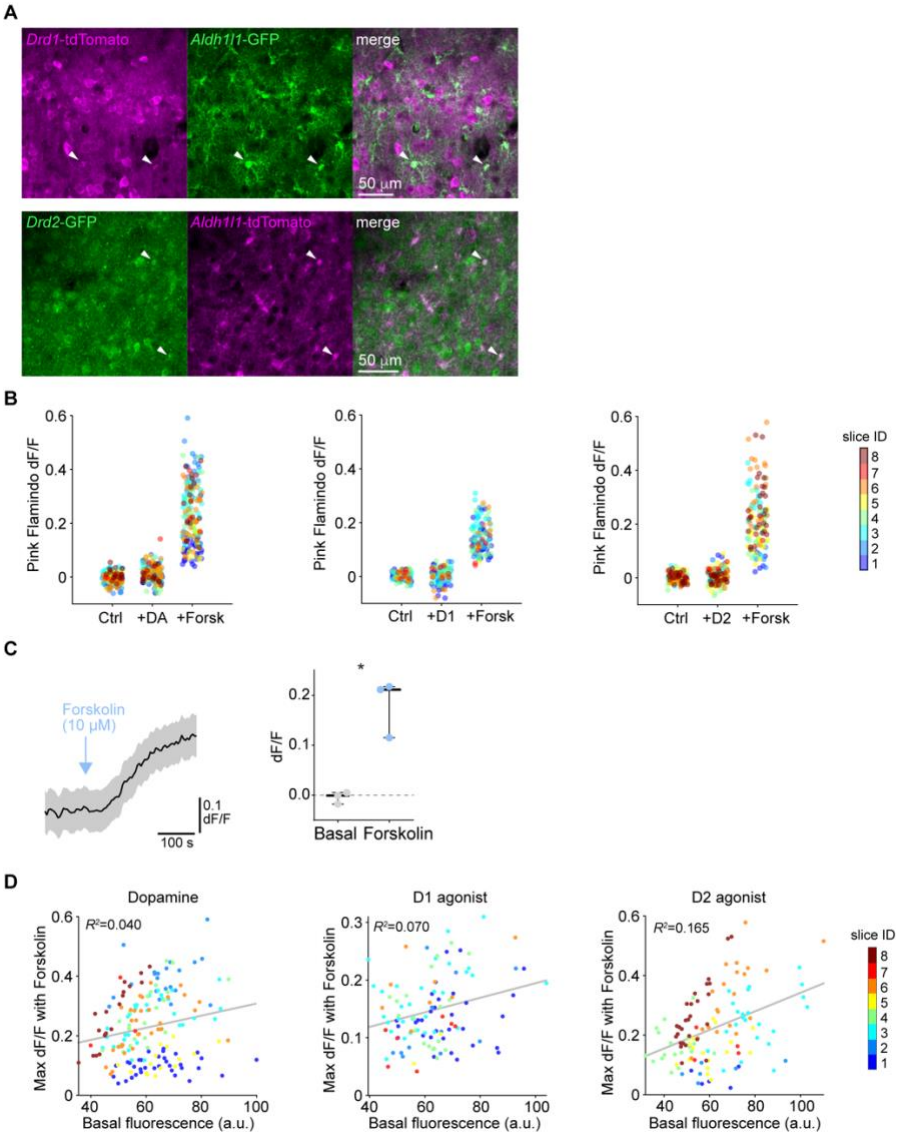

Figure S2, Controls for Pink Flamindo cAMP imaging, Related to Fig. 2. (A) Examples of high magnification (20x) micrographs from PFC of (top) *Drd1*-tdTomato x *Aldh1l1*-GFP and (bottom) *Drd2*-GFP x *Aldh1l1*-tdTomato mice to demonstrate colocalization and cell morphology. Arrowheads indicate cells co-expressing either receptor and Aldh1l1. **(B)** Fluorescence change from baseline for all analyzed cells, with colors indicating individual slices, to highlight no evident clustering of cells within individual slices. For the "+DA" condition, there is no evident separation of cells into two separate clusters, indicating that DA does not activate D1 (G_s pathway) and D2 receptors (G_i pathway) in different cells. Corresponding slice averages are shown in Fig 2G. **(C)** Adenylate cyclase activator Forskolin mobilizes cAMP in naïve slices, *i.e.* not treated with TTX and the drug cocktail to block neurons (right, Forskolin = 0.18±0.03 dF/F), at similar levels to those observed in treated slices (Fig. 2 F–G). Data shown as (left) mean traces±sem and (right) slice averages±sem of whole-cell Pink Flamindo fluorescence (dF/F) before (basal) and after Forskolin. Paired t-test; *, p=0.036; n=58/144 cells, 3 slices and mice. **(D)** Astrocytic response to maximal adenylate cyclase stimulation correlates weakly with cAMP reporter expression (Pink Flamindo basal fluorescence, arbitrary units). The observed variability in maximal cAMP concentrations in PFC astrocytes may reflect different signaling capabilities of individual astrocytes (*e.g.,* differential expression levels of AC subtypes, phosphodiesterases, *etc.*). Data are shown as cells (dots), colors indicate individual slice IDs. Pearson's coefficients (r^2) of linear correlation fits are indicated; p-values<0.007.

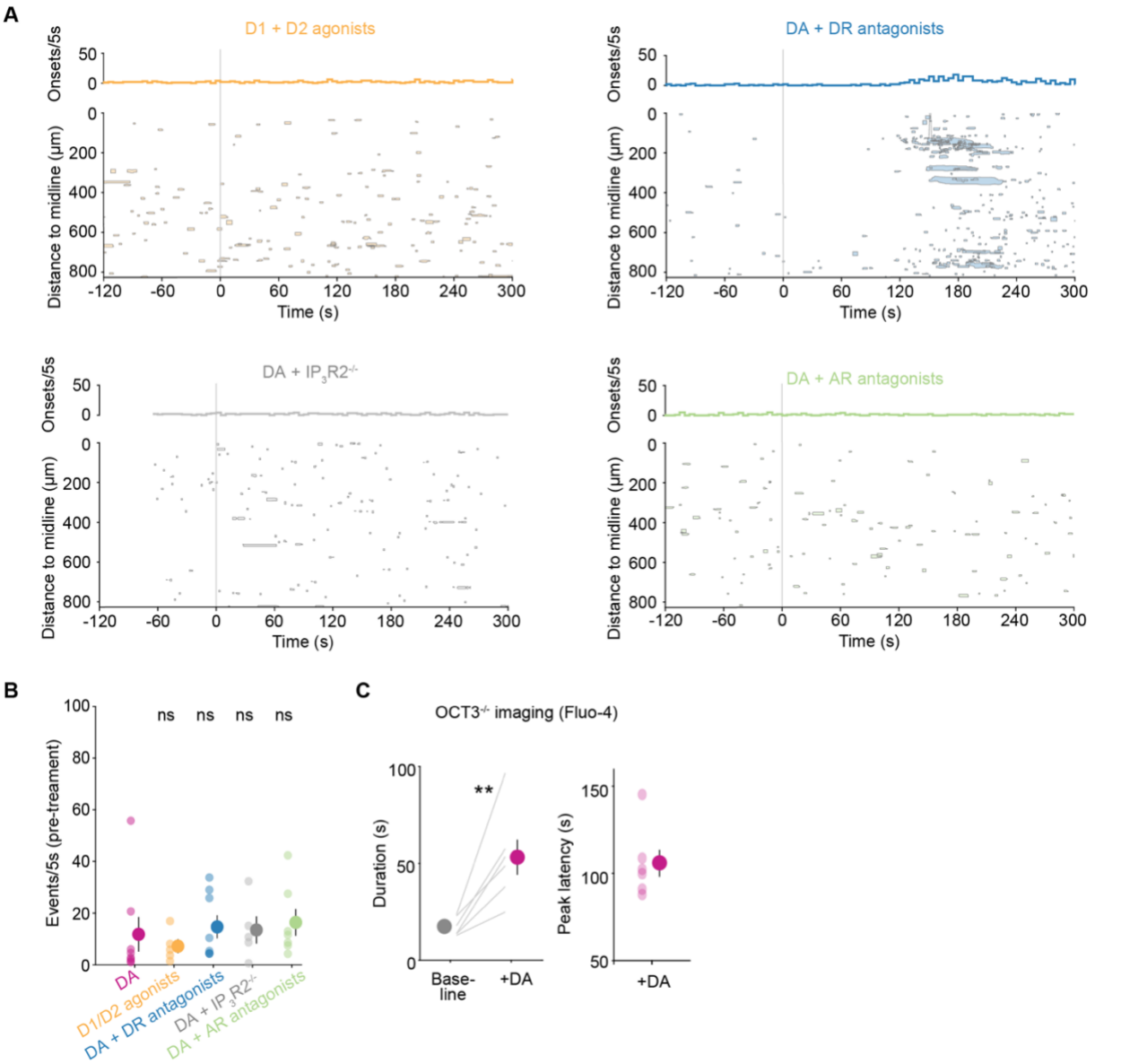

Figure S3, Expanded spatiotemporal plots and analysis of pharmacology in bath-application DA experiments, Related to Fig. 3. (A) Time course of astrocyte Ca^{2+} events detected in PFC slices relative to D1/D2 agonists application (SKF38393/Quinpirole, top left), or relative to DA application in D1/D2 antagonists (SCH23390/Sulpiride, top right), in IP_3R2 KO mice (bottom left), or in α-/β-AR antagonists (Phentolamine/Propranolol, bottom right), representative of data in Fig. 3E. Rate of event onset (counts in 5-s bins) is displayed on top of each graph. Shaded areas represent approximate event size and mean y-position of the event over time. **(B)** No difference in pre-treatment event rate (count/5 s) for all slices and conditions shown in Fig. 3E. Event rate was calculated over a 60-s period before treatment with DA or D1/D2 agonists (as indicated by x-axis labels). Data shown as all slices (transparent dots) and corresponding mean±sem (solid dot and error bar) for each condition): 11.8±6.7 (DA); 7.2±2.7 (D1/D2 agonists); 14.7±4.5 (DR antagonists); 13.5±5.3 ($IP_3R2^{-/-}$); 16.4±5.2 (AR antagonists). One-way Anova after Levene test; p=0.829; n=5–8 slices, 4–8 mice. **(C)** Average duration (left) and latency (right) of astrocytic somatic Ca^{2+} transients in slices from $OCT3^{-/-}$ mice imaged using Fluo-4. Duration of Ca^{2+} transients is higher after DA compared to that of spontaneous Ca^{2+} activity (basal). In $OCT3^{-/-}$ astrocytes, the latency to Ca^{2+} recruitment in response to DA is similar to that observed in wild-type mice (see Fig. 3D). Data shown as slice averages (lines or transparent dots) and corresponding means±sem (solid dots and error bars). Duration (s): 17±2 (Baseline); 53±10 (DA). Peak latency: 106±8s. Paired t-test after Anderson-Darling test; **, p=0.009; n=138 active cells, 6 slices, 3 mice.

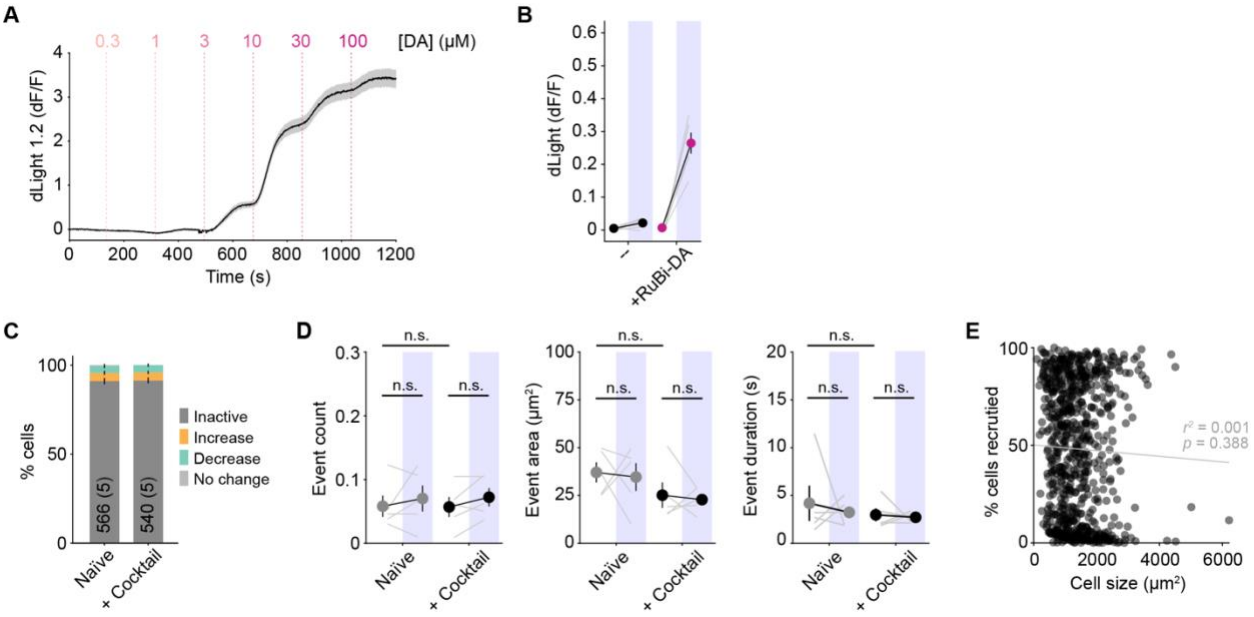

Figure S4, Validation of RuBi-DA photoactivation, Related to Fig. 4. (A) Representative dLight dose-response experiment as in Fig. 4C, showing time course of dLight fluorescence in slices challenged with increasing concentrations of DA (0.3 to 100µM, in 0.5-log steps; times of application indicated by dotted lines and corresponding concentrations shown on top). Data shown as mean±sem of different regions-of-interest selected across the imaging field. **(B)** dLight1.2 fluorescence before and after uncaging (30-s averages, data post-uncaging indicated by blue boxes) in PFC slices, in absence (--, black) or presence of RuBi-DA (magenta). Data from Fig. 4D, shown as slices (grey lines) and corresponding mean±sem (black lines, solid dots and error bars): 0.005±0.002, 0.022±0.005 (--); 0.007±0.001, 0.265±0.032 (+RuBi-DA). **(C)** Astrocytes were largely inactive (no Ca^{2+} events) before (naïve) and after addition of TTX and the multidrug cocktail (+ cocktail) used in all experiments in Fig. 4F–L. Percentage of cells increasing, maintaining, or decreasing their activity after the uncaging light pulse were low and similar between conditions, indicating no effect of light stimulation or drugs. Data shown as mean±sem; n=540–566 cells, 5 slices, 5 mice. **(D)** Ca^{2+} event features (number, area and duration) in active cells in (C) were unchanged after addition of TTX and multidrug cocktail. There was similarly no effect of the uncaging light (shaded blue boxes) on event features in naïve slices and those treated with the cocktail. Data shown as slice means (grey lines) and mean±sem (dots and error bars). After checking normality, the Wilcoxon rank sum test was used to compare event features before uncaging between naïve and cocktail, and the paired t-test used to compare event features pre- versus post-uncaging. Naïve: n=52/566 cells, 5 slices and mice. Cocktail: n=47/540 cells, 5 slices, 5 mice. **(E)** The maximum cell area recruited by fast release of DA shown in Fig. 4 J–L is independent of cell size, indicating that our cell delineation method does not affect this measurement. R^2, Pearson's coefficient, and p, p-value of linear correlation fit (grey line). N=1118 cells, 11 slices, 8 mice.

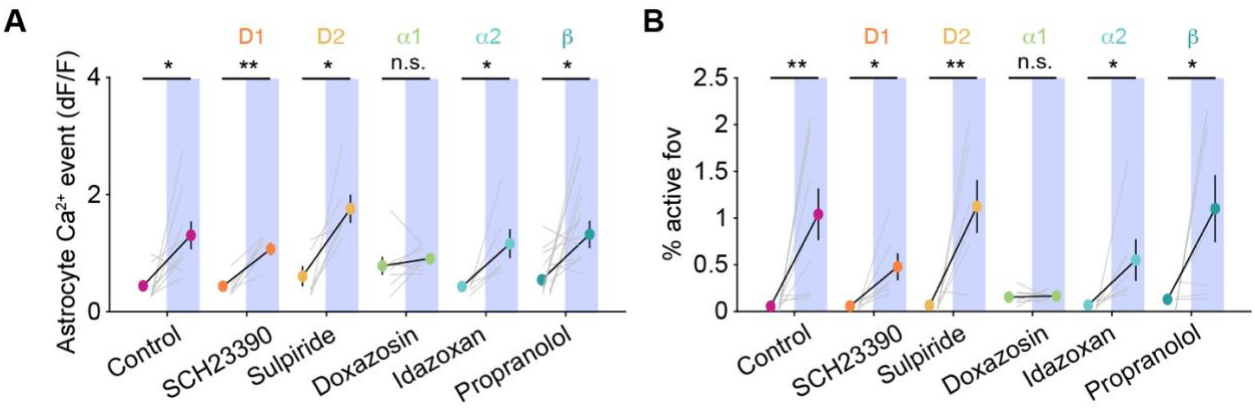

Figure S5, Alternate quantification of astrocyte Ca^{2+} response after DA uncaging, Related to Fig. 5. (A–B) Additional quantification of experiments in Fig. 5B yield comparable results to z-scored traces of AQuA Ca^{2+}-events (Fig. 5C). **(A)** dF/F traces of AQuA Ca^{2+}-events. **(B)** Percent of active imaging field recruited over time. Data shown as 30-s means of slice Ca^{2+} events immediately before or after RuBi-DA uncaging (shaded blue boxes) in presence of different receptor inhibitors as indicated, for slice averages (grey lines) and corresponding mean±sem (black lines, solid dots and error bars). One or two-tailed paired t-test or Wilcoxon signed rank test after checking normality with the Anderson-Darling test to compare pre- to post-uncaging values; *, $p<0.05$, **, $p<0.01$; n=6–9 slices, 5–9 mice.

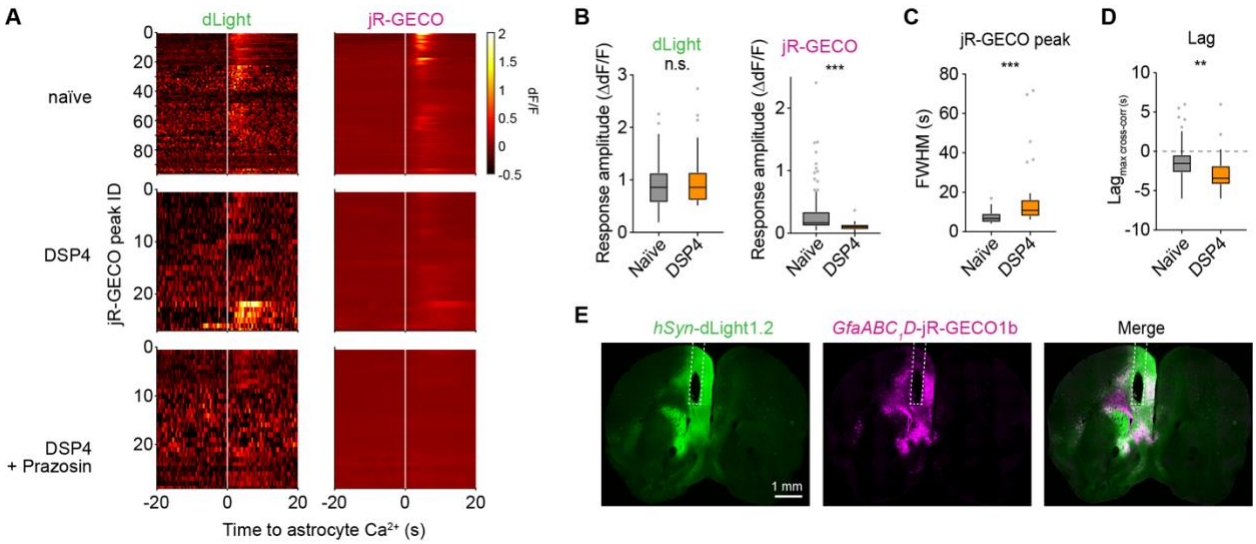

Figure S6: Fiber photometry controls with expanded data and analyses, Related to Fig. 6. (A) Fiber photometry recordings of dLight (left) and astrocytic jR-GECO (right) aligned to the onset of astrocyte Ca^{2+} transients evoked by aversive stimulation (t=0), shown as heat map of dF/F for all jR-GECO peaks detected and conditions in Fig. 6 (top: naïve; middle: DSP4; bottom: DSP4 and Prazosin). **(B)** Amplitude of DA transients (left, dLight) in PFC (naïve: 0.89±0.04 dF/F) was not significantly affected by ablation of LC fibers (DSP4: 1.02±0.11 dF/F), whereas astrocyte Ca^{2+} transients (right, jR-GECO) were significantly lower with decreased NE input (naïve: 0.31±0.04 dF/F; DSP4: 0.11±0.01 dF/F), indicating that the integrity of the NE system is important for astrocyte function in PFC. Data shown as Tukey boxplots. Wilcoxon rank sum test; ***, $p<0.001$; n=27–96 transients, 4–9 mice. **(C)** Astrocyte Ca^{2+} transients (jR-GECO peaks) were longer after decreased LC input to the PFC (naïve: 7.3±0.3 s; DSP4: 18.3±3.5 s). Data shown as Tukey boxplots. Wilcoxon rank sum test; ***, $p<0.001$; n=27–96 transients, 4–9 mice. **(D)** Lag of maximum cross-correlation between dLight and jR-GECO was significantly higher after decreased LC input to the PFC (naïve: -1.4±0.2 s; DSP4: -2.6±0.5 s). Data shown as Tukey boxplots. Wilcoxon rank sum test; **, $p=0.004$; n=27–96 transients, 4–9 mice. **(E)** Optic fiber implant location in PFC was confirmed by immunostaining ~2 mm rostral from Bregma to visualize expression of dLight (green) and jR-GECO1b in astrocytes (magenta), but note that implant location was determined initially by the stereotaxic coordinates.